Received: 27 December 2023 | Revised: 25 May 2024 | Accepted: 28 May 2024

DOI: 10.1111/bre.12878

Basin Research IAS EAGE WILEY

RESEARCH ARTICLE

Re-routing of submarine channels by Plio-Quaternary extensional tectonics along the Tanzania margin and implications for an offshore branch of the East African Rift System

Marina Dottore Stagna[1] | **Vittorio Maselli**[1,2] | **David J. Reynolds**[1] | **Djordje Grujic**[1] | **David Iacopini**[3] | **Pamela Reynolds**[1] | **Sugandha Tewari**[4] | **Arjan van Vliet**[5]

[1]Department of Earth and Environmental Sciences, Life Sciences Centre, Dalhousie University, Halifax, Nova Scotia, Canada

[2]Department of Chemical and Geological Sciences, University of Modena and Reggio Emilia, Modena, Italy

[3]Dipartimento di Scienze della Terra, dell'Ambiente e delle Risorse, University of Naples "Federico II", Naples, Italy

[4]Schlumberger SLB, Crawley, West Sussex, UK

[5]Shell, The Hague, South Holland, Netherlands

Correspondence
Marina Dottore Stagna, Department of Earth and Environmental Sciences, Life Sciences Centre, Dalhousie University, 6287 Alumni Cres, Halifax, Nova Scotia, B3H 4R2, Canada.
Email: m.dottorestagna@dal.ca

Funding information
Natural Sciences and Engineering Research Council of Canada (NSERC) Discovery Grant - RGPIN-2020-04461

Abstract

The distribution and timing of Neogene extensional structures along the offshore Tanzania margin and their influence on submarine sediment dispersal pathways remain poorly constrained. This knowledge gap limits understanding of the propagation of the East African Rift System (EARS) in the western Indian Ocean. In this study, we use 2D and 3D seismic reflection data to explore a portion of the upper slope region offshore the Rufiji River delta which led to the discovery of a new extensional structure. Horizon maps and seismic sections extracted from the 3D volume reveal that the slope was intersected by W-E-oriented turbidite channels during the Cenozoic until the early Pliocene (5.3 Ma). Since then, the opening of this graben, whose timing is also constrained by stratigraphic horizon flattening, has led to a southward reorientation of these channels, a pattern that persists today, as evidenced by the flow direction of the channels at the modern seafloor. 2D seismic profiles reaching depths of 10 s two-way travel time (TWT) indicate that the formation of this graben is not related to the reactivation of Mesozoic structures. In detail, seismic data show that the acoustic basement is intersected by extensional faults, likely related to the Jurassic rift tectonics, which is reactivated during the middle Cretaceous forming a gentle monocline. The lack of deformation in the post-Cretaceous suggests a period of tectonic quiescence which persists until the establishment of a new extensional regime responsible for the graben's opening, indicating a decoupling between Mesozoic and Neogene tectonics. Considering the similarity in kinematics, orientation and timing between the graben and other structures along the margin, onshore and offshore, we interpret this graben to be generated by a later tectonic phase of the EARS. These new results may indicate that tectonic stresses associated with the EARS

migrated from the Tanzania craton, where the oldest rift structures are dated to ca. 25 Ma, to the western Indian Ocean, where the tectonic activity started during the middle-late Miocene to Pliocene.

KEYWORDS

East African Rift System, Indian Ocean, Tanzania margin, tectonics, submarine sediment dispersal pathway, turbidite channels

1 | INTRODUCTION

Submarine channels are prominent geomorphic features that play a fundamental role in sculpting continental margins through erosional and depositional processes (Piper & Normark, 2001). These channels can extend across the seafloor for hundreds to thousands of kilometres (Covault et al., 2011, 2012; Piper et al., 1999; Talling et al., 2007), and may represent the primary conduits for the transport of land-derived materials (including sediments, organic carbon, pollutants and nutrients) to the deep marine environment (Heijnen et al., 2022; Shepard, 1936; Talling et al., 2015). The sediment flows (i.e., turbidity currents) that transverse them can also constitute a potential geohazard to seafloor infrastructures (e.g., pipelines, telecommunication cables; Carter et al., 2009, 2012; Talling et al., 2022), while their deposits may generate important reservoirs for hydrocarbon (Mayall et al., 2006; Weimer et al., 2000) or CO_2 storage (Gunter et al., 2004; Talling et al., 2023). Various factors influence the evolution of turbidite channels, including sea-level fluctuations, shifts in sediment supply and tectonic activity (Clark & Cartwright, 2009; Cohen & McClay, 1996; Deptuck et al., 2007; Kolla et al., 1980; Mutti et al., 2009; Piper & Normark, 2009). Among these, seafloor topographic alterations are of particular importance and can be driven by compressional, extensional and salt tectonics (Ferry et al., 2005; Gee & Gawthorpe, 2006; Huyghe et al., 2004; Mayall et al., 2010), or by other depositional and/or erosional processes (Bull et al., 2020; Dottore Stagna et al., 2023; Kneller et al., 2016; Martínez-Doñate et al., 2021; Qin et al., 2017; Wu et al., 2022). Therefore, understanding the relationship between seafloor deformation and channel evolution may be critical for deciphering tectonic events and their impact on deep-water depositional systems.

This study focuses on offshore Tanzania, the western Indian Ocean (Figure 1), where previous studies unveiled the presence of tectonic structures that may represent the offshore propagation of the eastern branch of the East African Rift System (EARS). Mougenot et al. (1986) were among the first to propose a link between the Kerimbas Graben and Davie Ridge with EARS tectonics (Figure 1b).

Highlights

- A NNW–SSE graben has been discovered offshore Mafia Island.
- Since the Pliocene, the graben reorientated southward the original W-E oriented turbidite channel system.
- During the Cretaceous, reactivated pre-existing faults formed a monocline, which did not obstruct the W-E sediment transport.
- This event was followed by a quiescent tectonic phase, interrupted by a new extensional phase from the Miocene.
- The opening of the graben occurred during Pliocene, and can be associated with the EARS.

More recent studies (Dottore Stagna et al., 2022; Maselli et al., 2019) have provided further evidence of the development of the offshore branch of the EARS, examining the evolution of submarine channel pathways from the Eocene to recent times. The availability of recently acquired seismic reflection data collected for energy exploration has allowed us to explore sectors of the margin that were so far poorly known, thus helping to improve our knowledge of the evolution of these offshore structures and how they influenced the margin's growth and sediment transfer towards the western Indian Ocean.

Here, we investigate a portion of the continental slope offshore the Rufiji River delta, just south-east of Mafia Island (Figure 2a), where the seafloor is affected by a previously unknown NNW–SSE oriented extensional structure which is being infilled by a sinuous turbidite channel. Our goal is to investigate the formation of this structure and how it controlled the evolution of slope channel systems over time to provide new constraints on the structural and stratigraphic evolution of the margin. By quantifying the timing of faults activity and changes in kinematics, we also aim to investigate whether the origin of this graben is linked to the EARS tectonics, thus providing new evidence to explain the extensional tectonics along the margin.

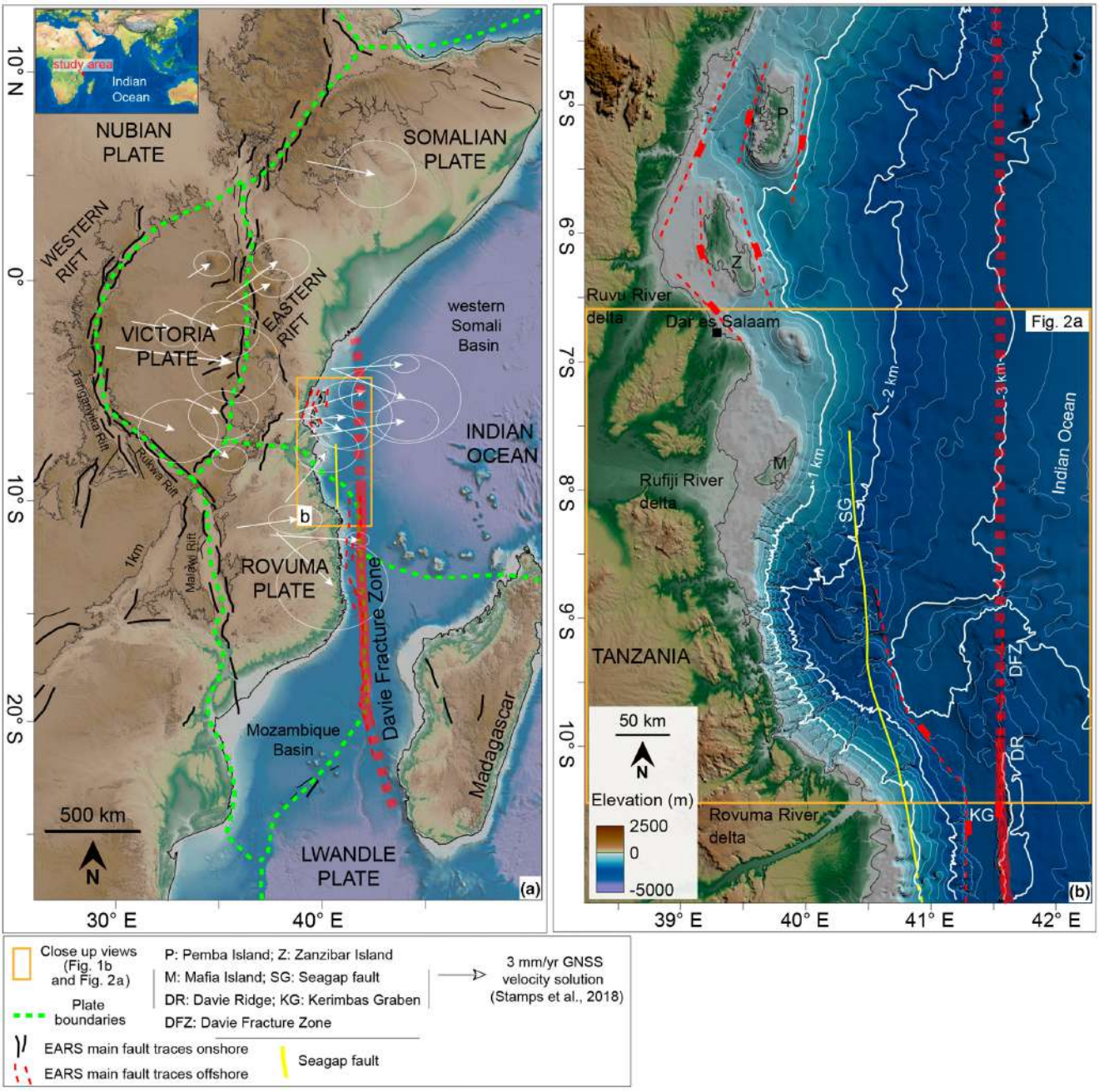

FIGURE 1 (a) The East African margin and tectonic framework, including the bathymetry of the western Indian Ocean, location of main structures onshore (in black) and offshore (in red) from Ebinger et al. (2024) and Iacopini et al. (2023), and plate boundaries in green dashed lines (Stamps et al., 2018). White arrows show the GNSS velocity data from Stamps et al. (2018). Orange square indicates location of the (b). (b) Bathymetric map of the offshore Tanzania. The map includes the location of offshore structures from Dottore Stagna et al. (2022) and Iacopini et al. (2023). Orange square indicates location of Figure 2a. DFZ, Davie Fracture Zone; DR, Davie Ridge; KG, Kerimbas Graben; M, Mafia Island; P, Pemba Island; SG, Seagap fault; Z, Zanzibar Island.

2 | GEOLOGICAL SETTING AND BACKGROUND

The origin of the Tanzania margin can be traced back to the middle Jurassic, when the breakup of the supercontinent Gondwana started, leading to the separation of East Africa and Madagascar together with India, Australia and Antarctica (Coffin & Rabinowitz, 1992; Jokat et al., 2021; Klimke & Franke, 2016). Synchronous seafloor spreading of the western Somali Basin (WSB) and Mozambique Basin since the late Jurassic (Figure 1a) led the initiation of the Davie Fracture Zone (DFZ), interpreted as transform dextral strike-slip fault system that accommodated the southward drift of

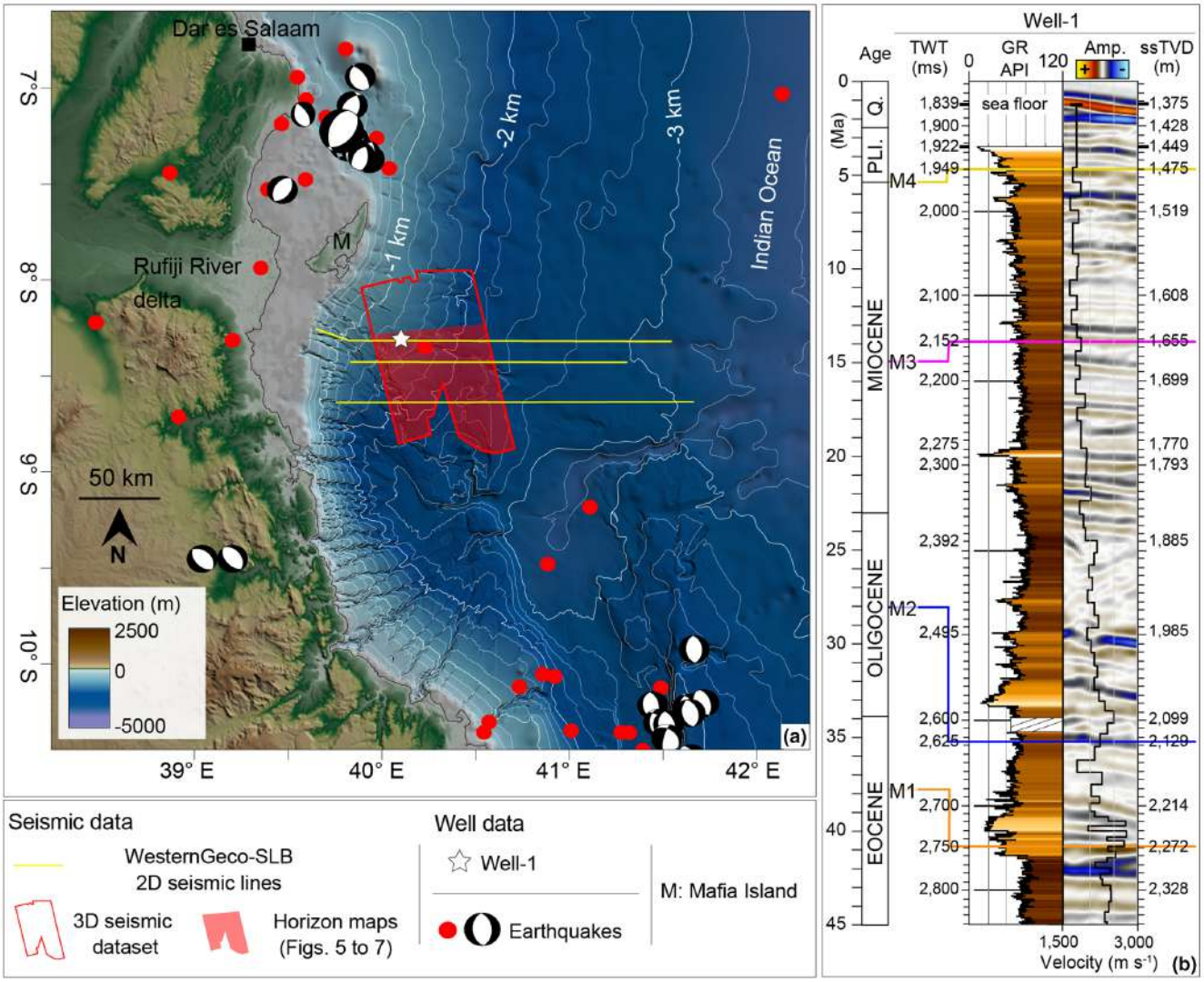

FIGURE 2 (a) Bathymetric map of the western Indian Ocean and study area location offshore Tanzania. The map includes the location of earthquakes recorded since 1980 from the USGS National Earthquake Information Center and ISC (International Seismological Centre), which are indicated with red circles (magnitude Mw ≥4) and Global Centroid Moment Tensor when available (see also Delvaux & Barth, 2010; Ekstrom et al., 2012). Red area indicates the location of the three-dimensional seismic data from Shell, with semi-transparent red colour indicating position of the realized surface maps (Figures 5–7; Supporting Information Figure S2); yellow lines indicate location of 2D seismic profiles from SLB; white star indicates the location of Well-1 in (b); (b) From left to right: dated stratigraphic horizons (M1–M4), Well-1 with gamma-ray log (GR), check-shots velocity model (black line), seismic reflection amplitude (Amp.), and depth in two-way travel time (ms TWT) and true vertical depth (m ssTVD).

Madagascar (Klimke & Franke, 2016; Mahanjane, 2014; Sauter et al., 2018; Sinha et al., 2019). The breakup between East Africa and Madagascar continued until ca. 90 Ma when the plate boundary between Africa and Madagascar became inactive (Reeves, 2018; Revees et al., 2016; Vormann et al., 2020) with Madagascar reaching its present-day position (Figure 1a; Klimke & Franke, 2016; Phethean et al., 2016). Mean-while, a new plate boundary formed between Madagascar and India (Reeves et al., 2016; Reeves, 2018), triggering intraplate deformations with pre-existing pre-Hautervian faults undergoing reverse faulting and inversion (Iacopini et al., 2023; Roche & Ringenbach, 2022; Sauter et al., 2018). After this drift phase, the relative position between Africa and Madagascar did not change (significantly) since (Figure 1a), and the onset of a relatively quiescent passive margin phase was established (Coffin & Rabinowitz, 1992; Reeves, 2018). The opening of the EARS started in the late Palaeogene in Ethiopia (Ebinger & Sleep, 1998), when a mantle plume developed below the thick cratonic African lithosphere, and then propagated southward for thousands of kilometres (Buitner, 2014; Burke, 1996; Ebinger & Sleep, 1998) and formed two branches (Figure 1a) synchronously during

the late Oligocene—early Miocene (ca. 25 Ma; Roberts et al., 2012).

Today, the EARS is a ca. 5000 km long divergent boundary along which the African Plate is in the process of splitting into two tectonic plates, called the Somali Plate and the Nubian Plate (Figure 1a; Stamps et al., 2021). The EARS encloses three smaller microplates, including Lwandle, Victoria and Rovuma (Figure 1a; Fernandes et al., 2013; Saria et al., 2014; Stamps et al., 2008), and the opening rates along the EARS range from less than 1 to 5.5 mm/yr (Stamps et al., 2021).

In this tectonic context, the formation of an offshore branch of the EARS was hypothesized along the Tanzanian margin (Bassias, 1992; Franke et al., 2015; Heirtzler & Burroughs, 1971; Iacopini et al., 2023; Kent et al., 1971; Mahanjane, 2014; Mougenot et al., 1986; Scrutton, 1978; Sinha et al., 2019; Vormann et al., 2020). Recent findings regarding the evolution of sediment dispersal pathways towards the western Indian Ocean and their link with the development of extensional structures along the margin (Figure 1b) provided additional evidence in favour of the hypothesis of the propagation of the EARS offshore. The post-Miocene offshore tectonics has led to the emplacement of a major mass-transport deposit offshore Mafia Island (the Mafia-mega slide; Maselli et al., 2020) reorganized the slope channels offshore Rovuma River delta (Maselli et al., 2019), and disconnected the deep-water drainage network from the feeding system offshore Zanzibar and Pemba islands (Dottore Stagna et al., 2022).

3 | DATA

3.1 | 2D and 3D seismic reflection data

We analysed 4225 km^2 3D post-stack, Kirchhoff time-migrated seismic reflection volume acquired by Shell and covering a total area of 6092 km^2 (Figure 2a) and cut at a depth of 4.5 s two-way travel time (TWT). The data are zero-phase and displayed with SEG normal polarity, indicated by an increase in acoustic impedance (peak) at the seafloor. The vertical resolution between the seafloor and horizon M1 is from 7.5 to 12.08 m, calculated considering a peak frequency of 60 Hz (frequency band spanning from 5 to 115 Hz) and interval velocity of 1800 to 2900 m/s, as derived from check shot data of Well-1 (Figure 2b, see also Maselli et al., 2020).

We also analysed ca. 570 km of 2D multichannel seismic reflection profiles (Figure 2a) from the Tanzania 1999/2000 Multiclient 2D survey (Figure 2a) acquired by WesternGeco-SLB using a 5200-m-long streamer with hydrophones at a 12.5 m interval. The seismic data were reprocessed by WesternGeco in 2012 introducing an anisotropic Kirchhoff pre-stack time migration. The seismic lines have been recorded to a depth of 10 s TWT.

4 | METHODS

The interpretation of seismic reflection data was conducted using Petrel software applying conventional methods of seismic stratigraphy and geomorphology (Mitchum et al., 1977; Posamentier & Kolla, 2003).

The stratigraphy presented here for the 3D seismic data is based on previous studies (Dottore Stagna et al., 2022; Maselli et al., 2020) that identified four key seismic horizons that were tied to Well-1 (Figure 2b) and named M1 (38 Ma), M2 (28 Ma), M3 (15 Ma) and M4 (5.3 Ma) (Figures 2b, 3 and 4; see also Supporting Information Figure S1). We used conventional terminology for the variation in acoustic impedance (Veeken & van Moerkerken, 2013) to describe the picked horizons: the term 'hard kick' indicates a downwards increase in acoustic impedance while 'soft kick' denotes a downward decrease in acoustic impedance. Surface maps have been made for the mapped horizons (Figures 5–8; Supporting Information Figure S2). The sinuosity index (SI) was estimated for the most recent turbidite channel at each seismic map (light green channels; Figures 5b, 6b and 7b). Root-mean-square (RMS) amplitude and edge detection variance seismic attribute maps were extracted for the horizon surfaces to image coarse-grained bodies (Figures 5c,d, 6c,d and 7c,d), such as turbidite channels, lobes and sediment waves, and discontinuities related to faulting and channels (Chen & Sidney, 1997; Chopra & Marfurt, 2007; Pigott et al., 2013).

Faults were manually picked throughout the 2D and 3D seismic datasets (Figures 3–7, 9 and 11), and detailed fault architectural elements, including segments and splays, have been visualized using edge detection seismic attribute variance (Figures 3d, 4d and 5d; Chopra & Marfurt, 2007). The fault lines for the 3D dataset were extracted from Petrel and imported into MOVE software, where fault planes were generated using the Delaunay triangulation method (Figure 9a; Delaunay, 1934). Strike and dip values were estimated for each of the faults, then classified based on their orientation and location and plotted to produce stereo plots and rose diagrams (Figure 9b). Since the seismic reflection data are in the time domain, the absolute values do not represent the real geometry of the faults but can be still used for structural interpretations as highlighted in other studies (see recent studies conducted in the area, e.g., Franke et al., 2015; Iacopini et al., 2023). We estimated a difference in the dip angle of the faults from TWT to depth by converting in depth the lower

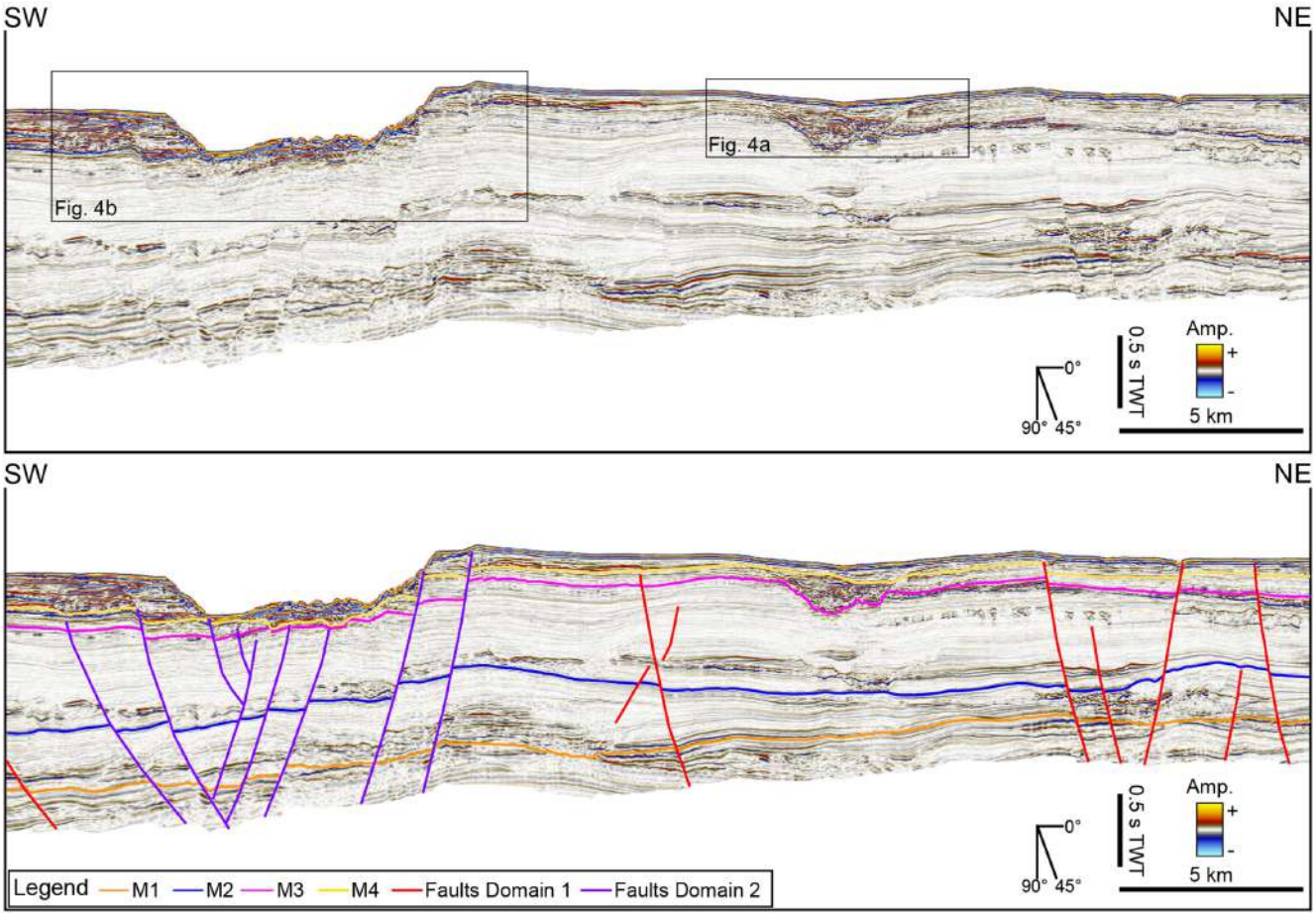

FIGURE 3 Uninterpreted and interpreted seismic line (vertical exaggeration 3:1) extracted from 3D seismic reflection volume (see location in Figures 5–7, 9 and 12), perpendicularly oriented to the strike of the faults (Figures 5–7 and 9). The interpreted version of the seismic line shows the four dated seismic horizons (age of the horizons provided in Figure 2b).

and upper tips of selected main faults affecting the seafloor and the lower portion of the seismic line in Figure 3 (see also Supporting Information Figure S1 for the same seismic line in 1:1 scale). The conversion has been achieved using the velocity at the seafloor (1800 m/s) and the deepest velocity value from the Well-1 (2400 m/s) (Figure 2b) and estimating the length of the faults through Pythagorean theorem and the trigonometric function of the sine of the dip angle. For the kinematic analysis, following the methods suggested by Allmendinger (2020), we calculated the mean vector of the poles of each group of planes and then the angle between those two mean vectors, which gave us the angle between the two conjugate fault sets. We kept in mind that σ_1 bisects the acute angle between the planes (the obtuse angle between the poles) and is perpendicular to the average line of intersection between the two groups of planes (Figure 9b; Supporting Information Figures S3 and S4 for analysis of stress inversion and faults from earthquakes, Delvaux & Barth, 2010, and Supporting Information Figure S5 for details on the kinematic stresses analysis).

Horizon flattening was used to estimate the timing of formation of the graben at the seafloor (Figure 10). This technique consists of selecting a seismic line perpendicular to the strike of the faults (Figures 3 and 10) and removing the deformation of picked horizons by shifting the data to a preselected reference horizon to a pre-deformation position (Bland et al., 2004). This enables the visualization and quantification of the displacement at the time of the selected reference horizon (Rouby et al., 1996, 2000).

Three additional horizons were selected for the interpretation of the deepest intervals imaged by the 2D seismic lines (Figure 11) based on the results of previous studies conducted in the same area (Franke et al., 2015; Sansom, 2018; Sauter et al., 2018; Scarselli, 2022). These horizons are: Base post-kinematic horizon (called Top Basement by Sauter et al., 2018, or Basement? by Scarselli, 2022); Base Cretaceous Unconformity (Sansom, 2018; also called Late Jurassic Unconformity by Franke et al., 2015) and Base Cenozoic (Scarselli, 2022; also called Base Tertiary Unconformity by Sansom, 2018).

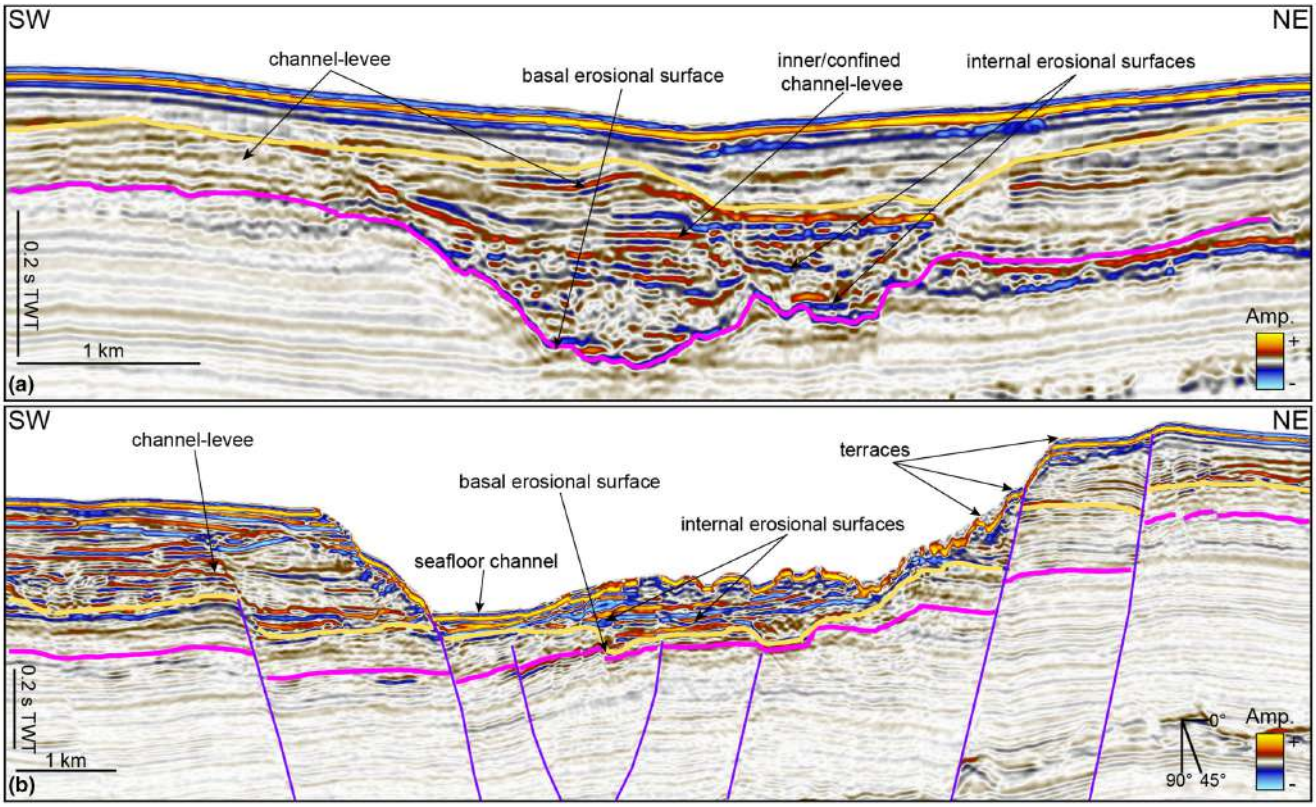

FIGURE 4 Zoom-in views of the channels from seismic line in Figure 3, with dated seismic horizons and faults, which provide details of interpreted erosional and depositional elements of the channel systems. Locations of (a) and (b) are indicated in Figure 3 by black squares.

5 | RESULTS

5.1 | Late Cenozoic horizons

The M1 horizon is a high-amplitude hard-kick seismic reflection and at places shows an erosional character as evidenced by reflection truncations (Figures 2b, 3 and 4). M1 ties with Well-1 at a true vertical depth below the sea level (ssTVD) of 2272 m (Figure 2b), giving a stratigraphic age of 38 Ma (Maselli et al., 2020).

Horizon M2 is characterized by a soft-kick reflection, laterally changing in amplitude (Figures 2b, 3 and 4) and intersects Well-1 at 2129 m ssTVD (Figure 2b). M2 has been dated to 28 Ma (Rupelian to Chattian; Maselli et al., 2020).

Horizon M3 is marked by a continuous to discontinuous hard-kick reflection with variable amplitude and mostly concordant with underlying stratigraphy except where it has been traced at the base of erosional turbidite channel systems or landslides (Figures 2b, 3 and 4). M3 ties with Well-1 at 1655 m ssTVD (Figure 2b) and has a stratigraphic age of 15 Ma (Maselli et al., 2020).

Horizon M4 is marked by a semi-continuous to discontinuous soft kick (Figures 2b, 3 and 4), laterally changing in amplitude and locally being eroded by more recent and/or active deep-water channels (Figure 4), which are also visible at the seafloor. It intersects the Well-1 at 1475 m ssTVD (Figure 2b), and it has been dated to 5.3 Ma (Maselli et al., 2020).

The seafloor horizon is a continuous positive/hard-kick, with high seismic amplitude and a continuous reflectivity (Figures 2b, 3 and 4). It is more U-shaped when incised by channels at the modern sea bottom, and wavier at the side of these channel incisions (Figure 4).

5.2 | Evolution of the submarine channels from Miocene to recent

We generated horizon surface maps for three mapped horizons: M3, M4 and the seafloor (Figures 5–7; Supporting Information Figure S2 for M1 and M2 horizon maps).

The surface map of horizon M3 exhibits a discontinuous appearance to the north, and a more homogenous-continuous to the south (Figure 5). In the north, we observe multiple incisions characterized in plain view by braided-like, straight to slightly sinuous morphologies, displaying a disorganized lateral migration pattern and poorly defined margins (Figure 5a,b). The

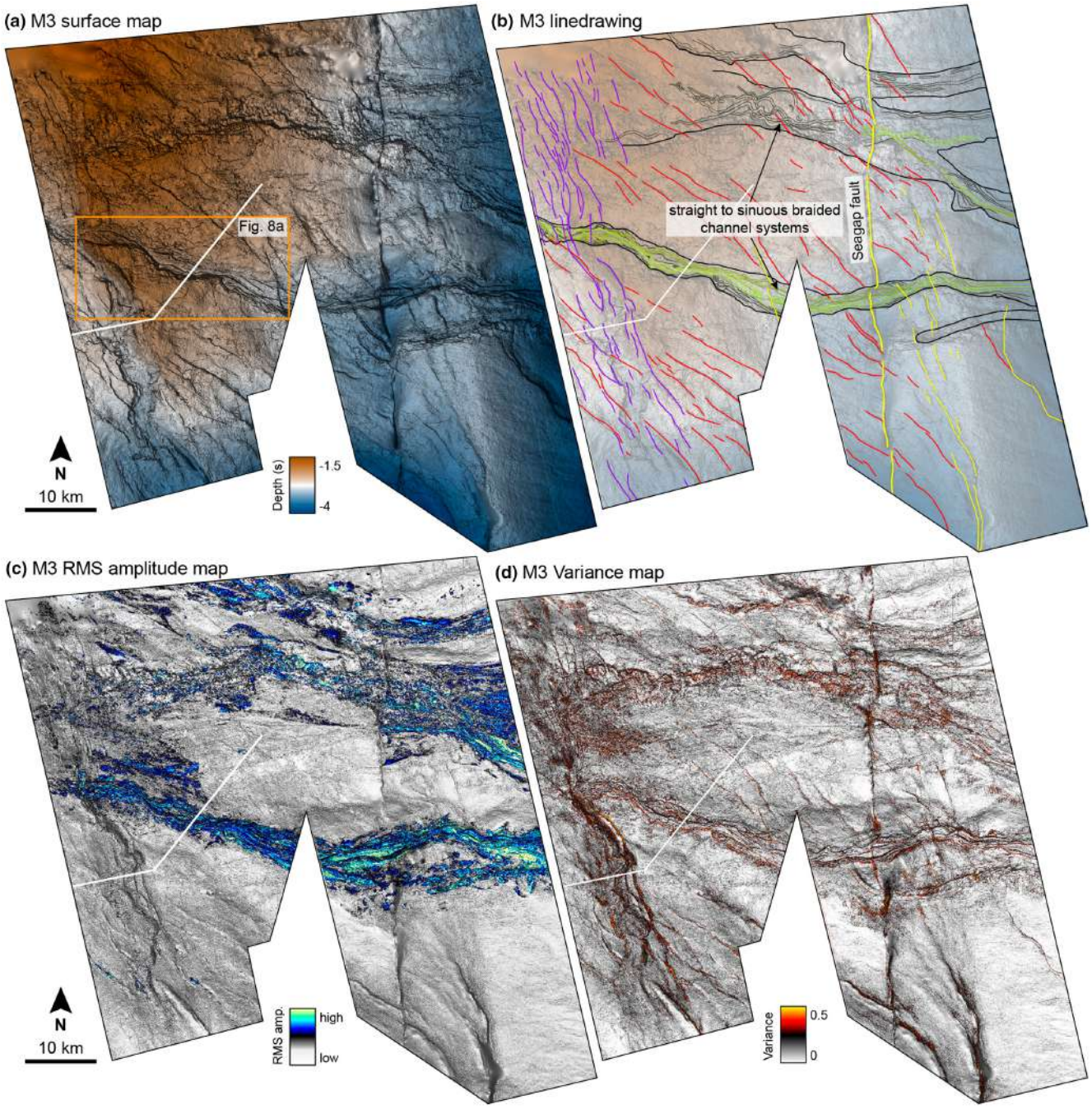

FIGURE 5 Surface elevation (a), line drawing (b), Root-mean square (RMS) amplitude (amp.) extraction (c) and Variance edge attribute extraction (d) maps of the horizon M3. Solid white line indicates the position of the seismic line in Figure 3. Solid green shade lines (b) show the position of the channel incisions, with the more recent being in a lighter colour. Solid black lines (b) are used to highlight other incisions which can be distinguished but only partially followed. Solid yellow lines: Seagap fault and related faults. Solid red lines: NW-SE fault domain 1 (Figure 9a). Solid purple lines: NNW–SSE fault domain 2 (Figure 9a).

high RMS amplitude response and overall morphology may indicate the presence of coarse-grained sediments (Figure 5c,d). In the central-south region of the surface map, localized multiple, slightly southward migrating, W-E oriented incisions are observed, still showing predominantly a disorganized lateral migration pattern but better-defined margins (Figures 5a,b and 8a). These incisions are more sinuous although still braided (SI: 1.07) and show a widening both moving from west to east and from old to more recent sequences, where they have better-defined margins. Some of the incisions in this region can be followed downslope for the entire

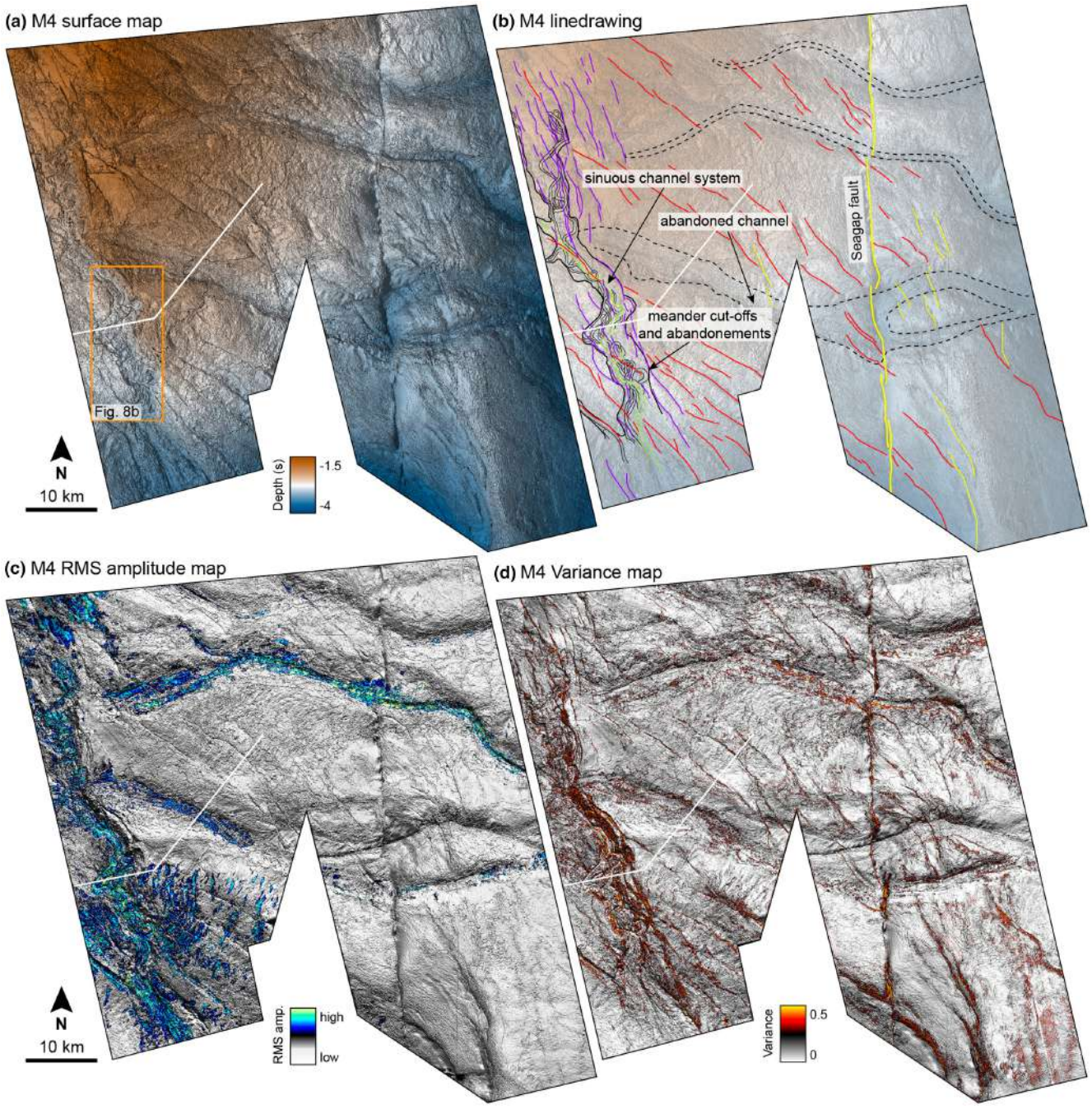

FIGURE 6 Surface elevation (a), line drawing (b), Root-mean square (RMS) amplitude (amp.) extraction (c) and Variance edge attribute extraction (d) maps of the horizon M4. Solid white line indicates the position of the seismic line in Figure 3. Solid green shade lines (b) show the position of the channel incisions, with the more recent being in a lighter colour. Solid black lines (b) are used to highlight other incisions which can be distinguished but only partially followed. Dashed black lines reveal the abandoned channels positions or successive incisions (b). Solid yellow lines: Seagap fault and related faults. Solid red lines: NW-SE fault domain 1 (Figure 9a). Solid purple lines: NNW–SSE fault domain 2 (Figure 9a).

map (Figure 5a,b), cutting across an area characterized by a low RMS seismic amplitude response (Figure 5c,d), which indicates that these channels incise fine-grained slope deposits (Figure 5). We assume that differences in imaging/visualization of the channels in the north and centre-south portion of the map are related to their emplacement on coarse- or fine-grained material (Figure 5c). In cross section (Figures 3 and 4a), we can observe that these incisions are characterized by high-to-medium amplitude, continuous to discontinuous

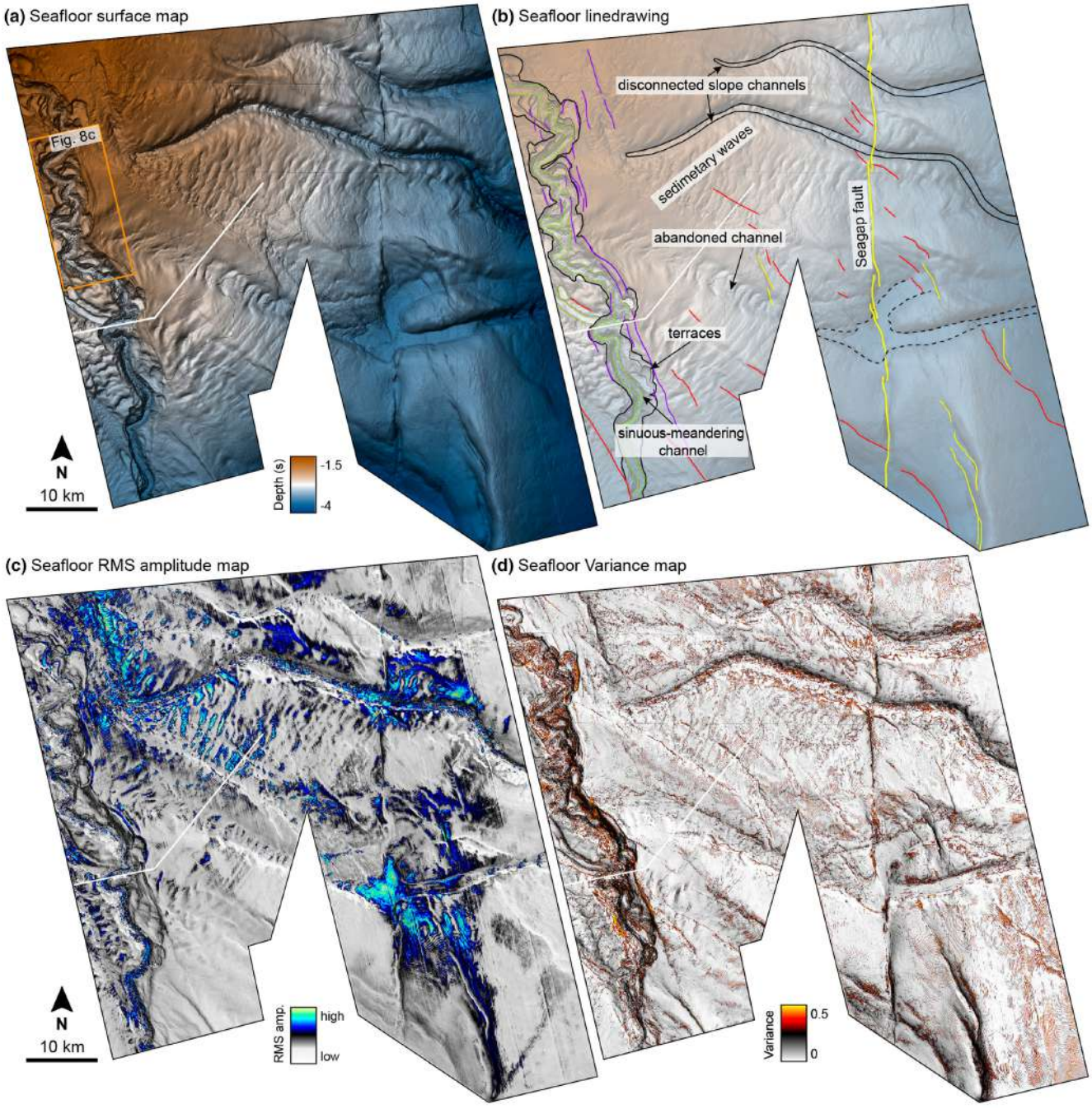

FIGURE 7 Surface elevation (a), line drawing (b), Root-mean square (RMS) amplitude (amp.) extraction (c) and Variance edge attribute extraction (d) maps of the seafloor horizon. Solid white line indicates the position of the seismic line in Figure 3. Solid green shade lines (b) show the position of the channel incisions, with the more recent being in a lighter colour. Solid black lines (b) are used to highlight other incisions which can be distinguished but only partially followed. Dashed black lines reveal the abandoned channels positions or successive incisions (b). Solid grey shade lines (b) highlight distinguished terraces. Solid yellow lines: Seagap fault and related faults. Solid red lines: NW-SE fault domain 1 (Figure 9a). Solid purple lines: NNW–SSE fault domain 2 (Figure 9a).

reflections, showing predominantly vertical disorganized stacking patterns, bounded and/or interrupted by erosional surfaces (Figures 3 and 4a). These units are flanked by more continuous and homogeneous seismic reflections that converge laterally (Figures 3 and 4a), thus suggesting the presence of drift/levees deposits. From the RMS and variance maps (Figure 5c,d), we do not observe high amplitude response N-S oriented on the western side, thus further demonstrating the absence of a NNW–SSE-oriented channel system at this time. Sediments with medium to high RMS amplitude response are visible towards the centre-eastern portion

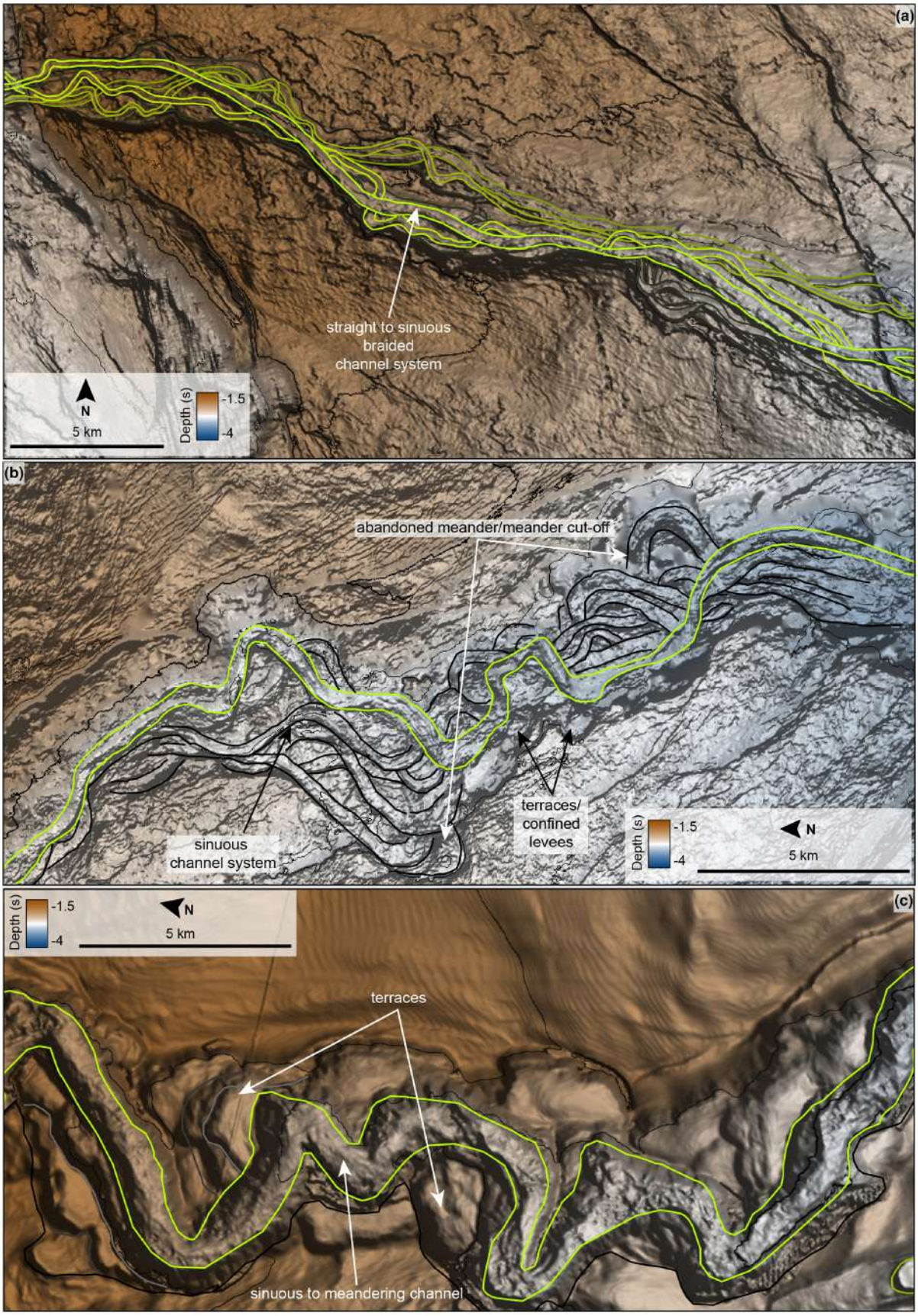

FIGURE 8 Close-up views of portion of the channels at horizon M3 (a), at horizon M4 (b) and at the Seafloor (c). Locations are indicated in Figures 5–7 by orange squares.

(Figure 5c,d), which is mostly dominated by low RMS amplitude and variance responses; the highest RMS values characterize the W-E-oriented channel fills. Overall, these channel-levees deposits are interpreted as mixed turbidite-contourite systems, as discussed by other studies in the region (Dottore Stagna et al., 2023; Fuhrmann et al., 2020).

The M4 surface map displays a similar discontinuous appearance to the previous M3 horizon map (Figure 6). However, the M4 surface reveals that older channels are now abandoned, and newly formed ones have oriented in a north–south direction (Figures 6 and 8b). These new channel systems exhibit similar characteristics but are more sinuous (SI: 1.3) to less braided when compared to the previous channel system (Figure 6a,b and 8b), with a sinuosity increasing southward, where it is also possible to observe meander cut-off and abandonments, resulting in the formation of multiple terraces and confined levees (Figure 3, 4b, 6a,b and 8b). To the north of the M4 surface map, west–east-oriented channels can be observed which are disconnected upslope (Figure 6).

On the western side, the seafloor surface shows a sinuous to meandering (SI: 1.55) north-northwest to south-southeast oriented channel (Figures 3, 4b, 7a,b and 8c). This channel erodes pre-existing incisions and leads to the formation of multiple terraces and confined levees (Figures 3, 4b, 7a,b and 8c). We can distinguish at least three phases of incision based on the terraces observed (Figures 4b, 7b and 8c). Additionally, west–east-trending submarine incisions are visible in the northern portion of the surface, and two of them are disconnected from the main sediment entry point upslope (Figure 7a,b) and interpreted to form due to overspill of sediments from the north–south-oriented channel. The previously observed incisional area in the southern portion of the surface is still preserved at the modern seafloor and is reactivated in the eastern deep-water region as disconnected slope channels (Figure 7a,b) that may be related to local instabilities of the slope. Overall, the seafloor surface map is more homogeneous, showing fewer incisions on the eastern side and a wavier appearance when compared to the previous surfaces (Figures 5–7). It is characterized by large, wavy, northward-trending elongated features associated with sediment waves, which suggest the ongoing presence of bottom currents along the Tanzanian margin (Figure 7).

5.3 | Fault distribution and kinematics in the post-Eocene interval

Faults were mapped through the 3D seismic dataset from a maximum depth of 4.5 s up to the seafloor and classified into two distinct fault domains (Figures 5–7 and 9; Supporting Information Figures S1 and S5).

The first domain (red faults; Figures 3–7 and 9) comprises NW-SE-oriented normal faults (Figures 5b–d, 6b–d, 7b–d and 9a) showing an extensional NE–SW kinematic (Figure 9b). The rose diagram exhibits petals oriented parallel to the strike with a mean value vector of 313° (±1.2°) for SW dipping faults and 133° (±1.6°) for NE dipping faults (Figure 9b). These faults are mostly moderate to high-angle normal faults, dipping both NE and SW (Figure 9b). NE dipping normal faults have an average of 48.7° (+25° for depth conversion) of dip, while SW dipping normal faults have an average of 42.9° (+23° for depth conversion) of dip (Figure 9). Kinematic analysis of faults of domain 1 (Figure 9b) highlights that stresses are σ1: 047/87, σ2: 313/01 and σ3: 223/03, which, according to the vertical stress principle (Anderson, 1905), highlight their extensional component. These faults detach from the pre-Oligocene units, are active from the middle Miocene (15 Ma) and, in some places, offset the seafloor indicating recent tectonic activity (Figures 3, 5b–d, 6b–d and 7b–d; Supporting Information Figure S1).

The second fault domain (violet faults; Figures 3–7 and 9) consists of NNW–SSE-oriented normal faults opening the NNW–SSE-oriented graben, with ENE-WSW extensional kinematic (Figures 5b–d, 6b–d, 7b–d and 9a). NNW–SSE faults have an arcuate orientation which terminations may indicate the presence of relay structures. These faults dissect the previously mentioned NW-SE-oriented faults (Figures 5b–d, 6b–d, 7b–d and 9a) indicating that they are the result of more recent tectonic activity. The rose diagram shows petals parallel to the strike direction with a mean value of 320° (± 2.7°) for WSW dipping faults and 158° (±1.6°) for ENE dipping faults (Figure 9b). ENE dipping normal faults have an average of ca. 50.1° (+15° for depth conversion) of dip and WSW dipping normal faults have an average of ca. to 38.2° (+16° for depth conversion) of dip (Figure 9b). Kinematic analysis of faults of domain 2 (Figure 9b) highlights that stresses are σ1: 114/79, σ2: 332/09 and σ3: 241/07, which shows that the area is in extension (extensional tectonic regime). Furthermore, we observe a ca. 20° rotation of principal stress axes between the two domains (Figure 9b), but even for domain 2, they are ca. 30° from the earthquake-derived values (Delvaux & Barth, 2010; see also Figures S3 and S4) in the area, thus highlighting decoupling with deeper structures. Similar to the first domain, faults of domain 2 detach within the pre-Oligocene units and offset the seafloor indicating recent tectonic activity (Figures 3, 5b–d, 6b–d, 7b–d; Supporting Information Figure S1). Although there is no observed evidence of

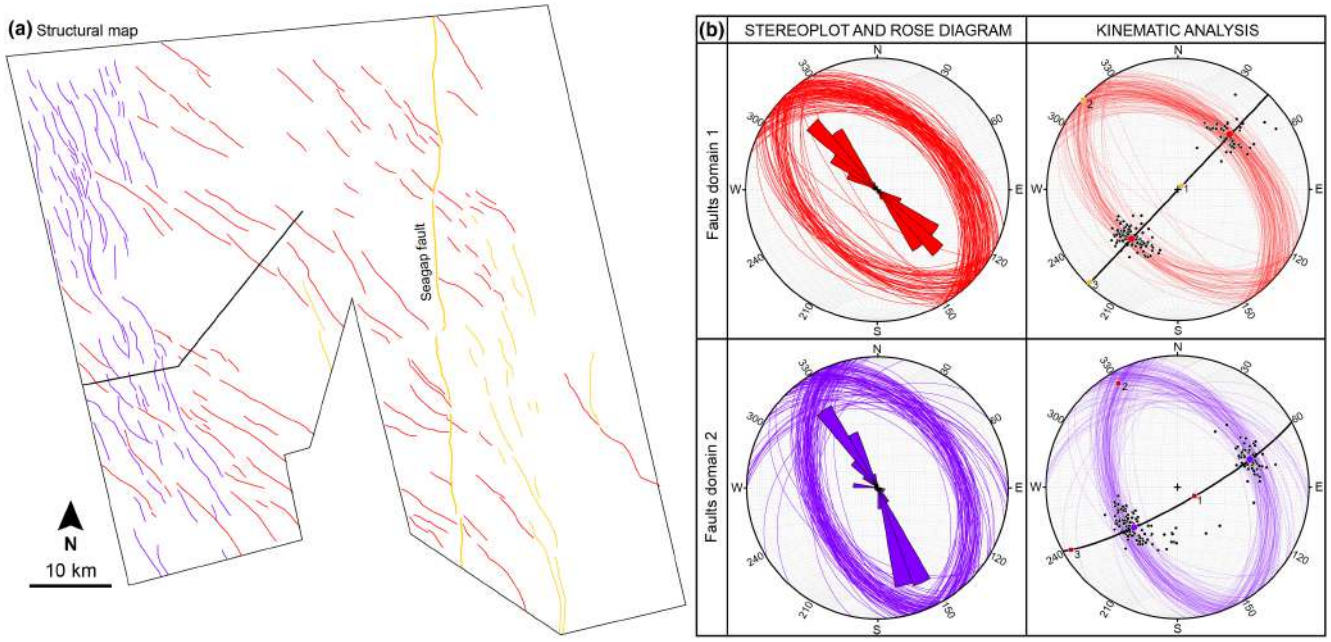

FIGURE 9 (a) Structures map of the study area, illustrating fault traces as lines. Red lines indicate faults from Fault domain 1 (b), while purple lines are faults of the graben (Fault domain 2, b). Yellow lines are fault traces associated with the Seagap fault system, and these are not included in (b) plots. (b) Stereoplots, rose diagrams and kinematic analysis of the two fault domains (1: σ_1; 2: σ_2; 3: σ_3). For Fault domain 1, poles of each group of planes are indicated by black dots and mean vector of the poles to each group of planes are indicated by red dots, while stresses (σ_1, σ_2, σ_3) are indicated with orange squares. For Fault domain 2, poles of each group of planes are indicated by black dots and mean vector of the poles to each group of planes are indicated by violet dots, while stresses (σ_1, σ_2, σ_3) are indicated with dark red squares.

syn-deposition, also due to the erosion generated by the channel flowing within the graben between the M4 horizon and the seafloor (Figures 3 and 4), the fault activity is inferred to have commenced during the early Pliocene, around the time of the M4 horizon (early Pliocene time, 5.3 Ma) because of the deviation of the channel system occurs at this time (Figures 5b–d, 6b–d, 7b–d). These faults are predominantly located in the westernmost part of the study area, offshore the southern portion of Mafia Island (Figures 5b–d, 6b–d, 7b–d). Seismic data show that these faults generate horst-graben and half-graben structures (Figure 3 and Supporting Information Figure S1), thereby confirming the extensional component in the area during this time (Figure 9b).

5.4 | Timing and evolution of the graben offshore Mafia Island

Horizon flattening was applied along horizons M1, M2, M3, M4 and the seafloor to understand the timing and evolution of the graben offshore Mafia Island (Figure 10).

Flattening of the horizons M1 and M2 (Figure 10a,b) provides a representation of the pre-tectonic deformation offshore: below the flattened M1, the reflectors are horizontally layered within the Eocene sequence (Figure 10a) and the same is observed at the flattening of the M2 horizon, with the pre-Oligocene sequence being continuous across the graben (Figure 10b). Changes in thickness between M1 and M2 horizons are associated with northward elongated levees or due to the erosive component of the M2 surface (Figure 10b). Minor irregularities observed near major faults of the graben were not caused by deformation but are rather related to depositional and erosional processes.

Flattening of horizon M3 reveals mostly horizontal reflections in the graben location, with only minor displacement noticeable for faults located on the east side of the graben and the eastern side of the seismic line outside the graben (Figure 10c). The uplift in the middle of the section is an artefact generated by the restoration of the real incision visible in that position (Figure 10c). Changes in

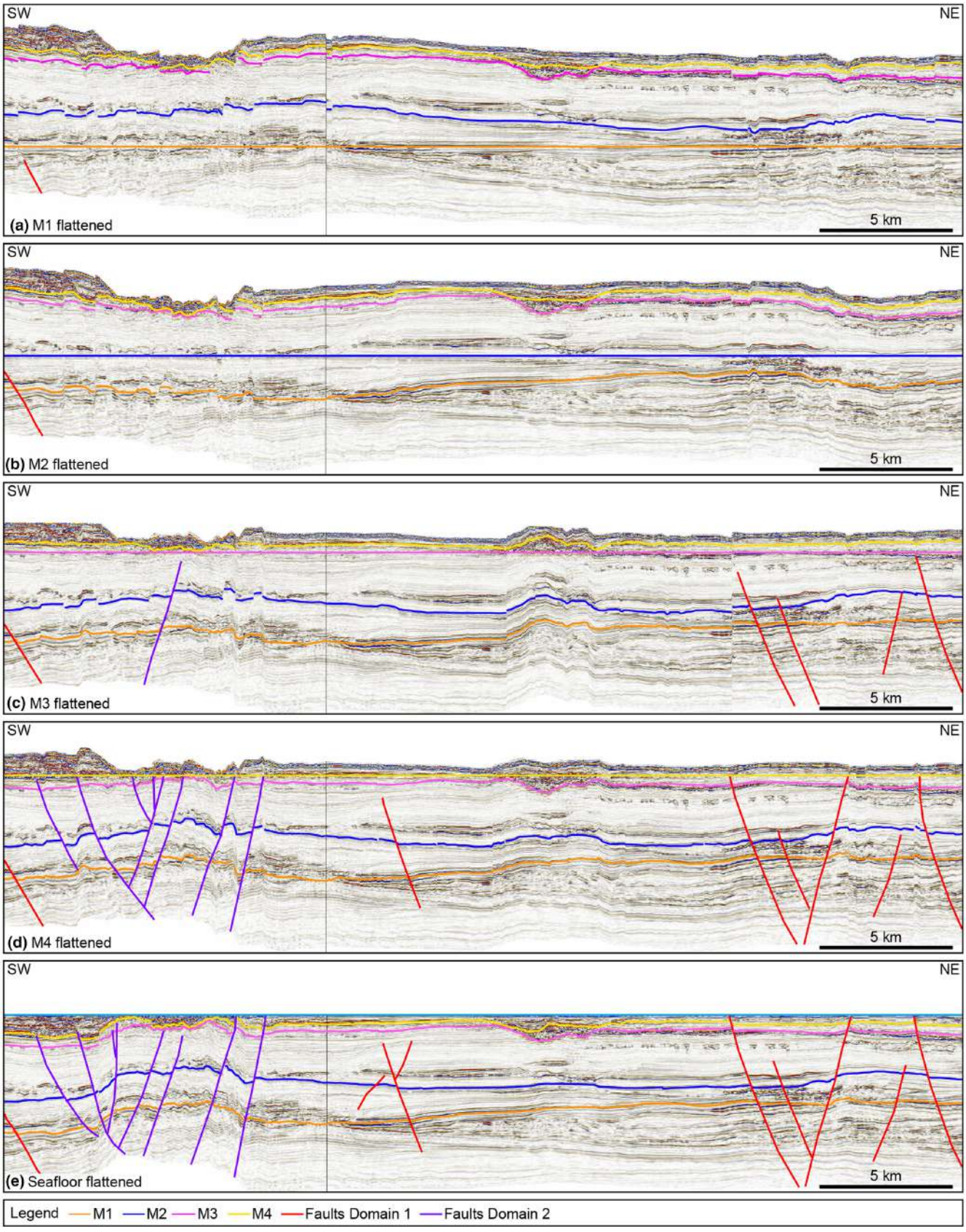

FIGURE 10 Horizon flattening across the studied graben. In red and purple are the faults considered to be active at the time of the flattened horizon. (a) M1 horizon (38 Ma) flattened; (b) M2 horizon (28 Ma) flattened; (c) M3 horizon (15 Ma) flattened; (d) M4 horizon (5.3 Ma) flattened; (e) Seafloor flattened.

thickness between M3 and the previous horizon M2 are again associated with the erosive component of the surface M2 and erosive features such as channels above the M2 horizon.

Flattening of horizon M4 shows the initial stage of the graben development on the western side of the seismic section (Figure 10d) where M1, M2 and M3 horizons start to be displaced. By ignoring the artefacts arising from the deformed horizon, it becomes evident that the surfaces are mostly undisturbed on the eastern portion of the seismic line, except where the deformation was already taking place (Figure 10d). There is no evidence of syn-deposition in the eastern portion of the seismic line, while in the western graben, a change in thickness is visible between horizon M3 and M4, which may be associated with the erosive component of the M4 surface (Figure 10d).

When flattening the seafloor horizon, we can observe that most of the deformation of the graben occurred more recently (Figure 10e). A distinct depocentre on the western side between the M4 and seafloor horizons can be associated with channel deposits and levee-drifts (Figure 10e). However, due to the presence of the modern channel at the seafloor, it becomes challenging to infer any evidence of syn-deposition.

5.5 | Mesozoic horizons, units and structures

In the 2D seismic reflection data, the deepest mapped horizon, named the Base post-kinematic horizon (called Top Basement by Sauter et al., 2018), is marked by a discontinuous/semi-continuous hard-kick characterized by high-to-medium seismic reflection amplitude (Figure 11a,b). This horizon separates chaotic to semi-continuous, wedge-shaped seismic reflection packages below (Figure 11c1,c2), from onlapping to continuous parallel reflections above. We interpret this horizon to represent the base of the post-rift sequence, located above syn-deposition (Karoo-age sedimentary sequence), as also discussed in Franke et al. (2015) and Sauter et al. (2018). The acoustic basement is located below the syn-rift deposits and marked by a discontinuous hard-kick, at parts corresponding to the Base post-kinematic horizon (Figure 11a,c1,c2). The thickness in between this horizon and the Base Cretaceous Unconformity is overall constant, with localized variations related to deep rift structures (Figure 11a,b).

The Base Cretaceous Unconformity (Sansom, 2018; also called Late Jurassic Unconformity by Franke et al., 2015) is characterized by a continuous hard-kick, high-to-medium seismic amplitude reflection, which truncates pre-existing seismic reflection packages (Figure 11a,b). It was interpreted to mark the passage from rifting to transform-controlled passive margin development (Franke et al., 2015; Sauter et al., 2018). Localized changes in thicknesses between the Base Cretaceous Unconformity and the Base Cenozoic appear to be depositional-related (Sansom, 2018), while the overall thickness is nearly constant (Figure 11a,b).

The Base Cenozoic (Scarselli, 2022; also called Base Tertiary Unconformity by Sansom, 2018) is characterized by a wavy, semi-continuous soft-kick, high-to-medium seismic amplitude reflection (Figure 11a,b). Below the Base Cenozoic horizon, we can observe onlapping reflections at a depth of ca. 1.5 s TWT above the Base Cretaceous Unconformity (Figure 11d1,d2) and an overall change in dip of the reflections along the seismic line moving from west to east (Figure 11a,b), with the reflections being horizontal-to-west dipping and then changing to slightly east dipping at ca. 20 km moving eastward from the left beginning side of the seismic line. This suggests the presence of a smooth monocline (Figure 11a,b), a sub-cylindrical fold that exhibits a single smoothly west-inclined limb in an overall flat or gently east-dipping sequence. An increase in thickness can be observed between the Base Cenozoic horizon and the seafloor, mostly on the western side of the seismic section, while thickness decreases eastward (Figure 11a,b).

The graben is bordered and dissected by east- and west-dipping high-angle faults, which displace parallel continuous medium to low seismic reflection amplitude in the upper section (Figure 11a,b). These normal faults dissect most of the sequence above the Base Cenozoic: some of the normal faults splay from two high-angle master faults, respectively, east- and west-dipping (Figure 11a,b). Some of the largest faults detach at a depth of ca. 1 s TWT above the Base Cretaceous Unconformity (Figure 11a,b), dissecting the Base Cenozoic horizon but do not affect the Base Cretaceous Unconformity horizon, thus showing their independence from pre-existing deeper faults. This indicates that the monocline formed before the shallowest faults.

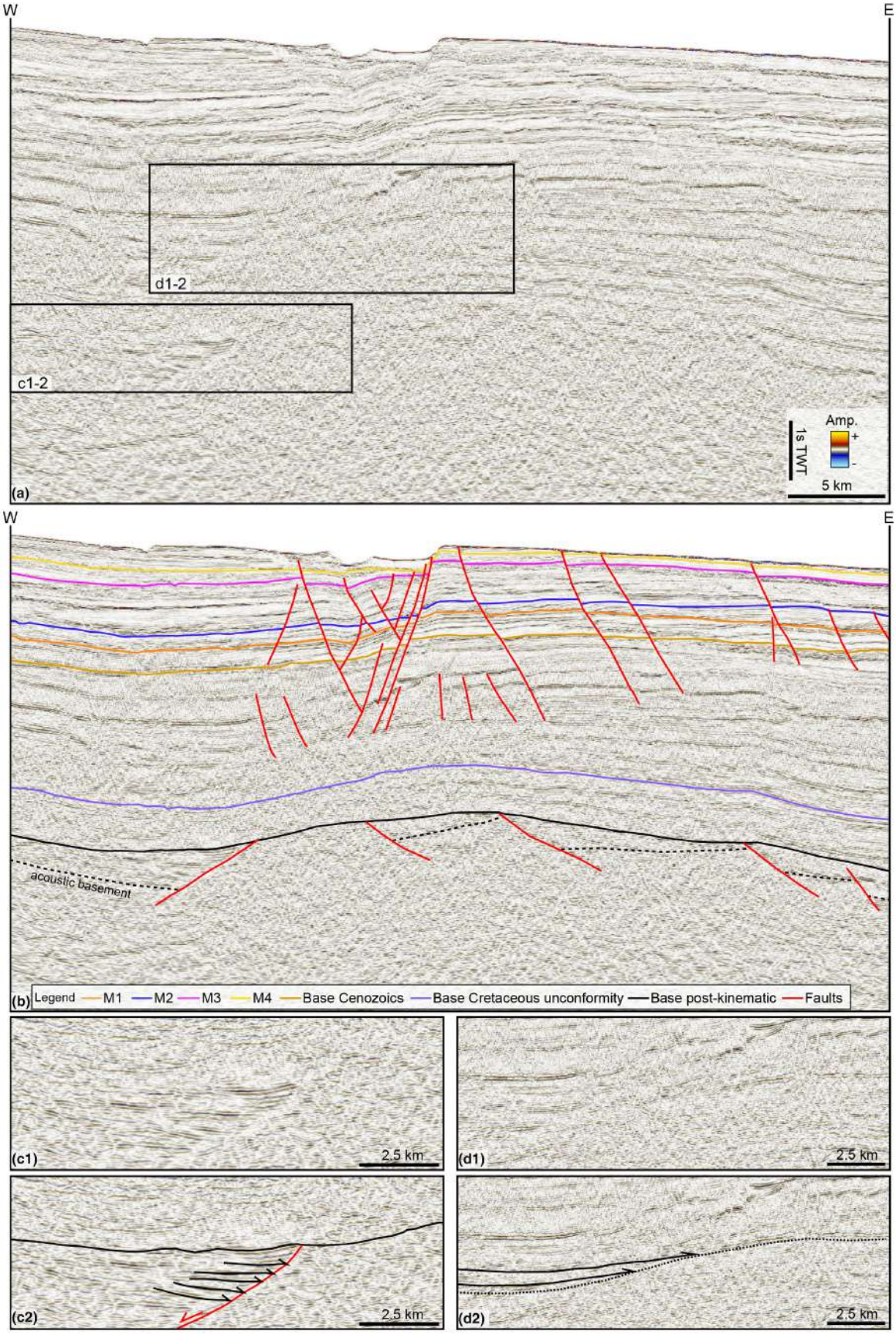

FIGURE 11 2D seismic reflection line from SLB, both non-interpreted (a) and interpreted (b). Two black rectangles in (a) indicate the location of the two close-up views located at the bottom of the figure (c, d). Black arrows: onlaps. Dashed black lines: acoustic basement.

6 | DISCUSSION

6.1 | Correlation between shallow and deep structures

To evaluate whether the tectonic activity giving rise to the graben is associated with the reactivation of pre-existing structures, we analysed 2D seismic reflection profiles and explored any link between Neogene and Mesozoic structures (Figure 11). Folded reflections between the Base post-kinematic and the Base Cenozoic horizons form a monocline gently dipping westward. The lateral distribution of the reflections is predominantly horizontal and continuous, with folding becoming evident at the limb location (Figure 11), where the reflections smoothly dip westward. Particularly, onlapping reflections occur at the limb and the hinge in between the Base Cretaceous Unconformity and the Base Cenozoic horizons (Figure 11d). Furthermore, data show that the monocline coincides with underlying extensional basement faults and uplifted basement (Figure 11a,b). Based on the reflections' terminations and thickness distribution, we speculate that the folding/basement uplift occurred after the Base Cretaceous Unconformity and probably during the Cretaceous (middle-late Cretaceous). Shallower extensional structures above the monocline are decoupled from the fold itself (Figure 11). Normal faults above the monocline form a NNW–SSE graben, ca. 180 m deep and ca. 5.55 km wide at the modern seafloor (Figure 3). These faults detach at a depth of ca. 0.5 s from the tip of the monocline into the Cretaceous unit (Figure 11) from muddy prone deposits (Sansom, 2018; see also Supporting Information) and dissect the Cretaceous and Cenozoic sequences up to the seafloor without evidence of syn-growth deposition (Figures 3 and 11), thus suggesting decoupling and a phase of tectonic quiescence offshore from late Cretaceous until Miocene. The absence of syn-growth deposits suggests very recent extensional tectonic activity, at least from the Pliocene to recent times, in agreement with the results of the flattening analysis (Figure 10).

It is well known that the East African margin was built over multiple episodes of reactivations (both extensional and compressional) of pre-existing structures and deep structures were overprinted by the more recent tectonic activity of the EARS (Dottore Stagna et al., 2022; Franke et al., 2015; Iacopini et al., 2023; Sii & Underhill, 2015). Monoclines can develop above blind faults (see Ameen, 1988; Beloussov, 1959; Ferrill et al., 2007; Hardy & McClay, 1999; Hudson, 1955; Prucha et al., 1965; Sandford, 1959; White & Crider, 2006; Willsey et al., 2002), and although a detailed understanding of the mechanisms forming the monocline is beyond the scope of the paper, we propose two models that can explain the monocline's growth considering the tectonic setting of the area. The first model implies an extensional fault propagation folding through normal reactivation of a pre-existing west-dipping fault developing at the tip of propagating normal faults (e.g., Ferrill et al., 2012; Gawthorpe et al., 2003; Jackson et al., 2006; Patton, 1984; Stearns, 1978; Tavani et al., 2013), thus generating upward-widening monoclines (Gawthorpe et al., 1997; Janecke et al., 1998; Khalil & McClay, 2002; Schlische, 1995; Willsey et al., 2002). Alternatively, the formation of the monocline can be related to the inversion of a pre-existing east-dipping normal fault forming a fault propagation fold (Erslev, 1991; Hardy & Finch, 2006; Suppe & Medwedeff, 1984; Tindall & Davis, 1999). Similarly to the study area, extensional structures in shallower stratigraphic units that are decoupled from deeper structures have been observed to form at the upper inflexion point of a monocline (Pascoe et al., 1999; Vendeville et al., 1995), some distance away from basement faults and in the direction of the uplifted block (Vendeville, 1987, 1988; Vendeville et al., 1995; Withjack et al., 1990). In such systems, the degree of decoupling between deep and shallow structures typically depends on the planar anisotropy of the units involved in the deformation (Keller & Lynch, 1999; Stearns, 1978; Vendeville, 1987; Withjack et al., 1988, 1989). In the study area, sediments between the Base Cretaceous Unconformity and Base Cenozoic horizons consist of mud-dominated contourite drifts and turbidite fans affected by along slope currents (Sansom, 2018) covered predominantly by coarse-grained gravity flow deposits which can explain the decoupling between the Mesozoic and Neogene structures (see Supplemental Materials—Angle of internal friction).

Decoupling between shallow and deep structures can be further demonstrated by comparing the stress field within the study area (Delvaux & Barth, 2010; Figure 9b and Supporting Information Figures S3–S5). We observe that σ_1 is vertical (or quasi-vertical), while σ_2 and σ_3 are sub-horizontal, which, according to the vertical stress principle, indicates that the area is affected by an extensional tectonic regime. Fault slip analysis and the plot of the poles to the faults (Delvaux & Barth, 2010; Supporting Information Figures S3 and S4) show radial extension in the deep section according to the earthquake data in the study area (Delvaux & Barth, 2010), while the analysis of shallower faults (Figure 9b) highlights a pure extensional regime. Analysis of the principal stress axes shows that there is ca. 20° rotation of principal stress axes between the two domains and a ca. 30° rotation of principal axes of fault domain 2 and the earthquake-derived values (Figure 9b and Supporting Information Figures S4 and S5) that further agrees with our decoupling hypothesis between shallower and deeper structures. The fault plane

solution shows predominantly a W-E extension (Supporting Information Figure S4), in agreement with what has been observed from the plot (Figure 9) and with the more regional stress regime (Delvaux & Barth, 2010).

6.2 | Tectonic influence on turbidite channel pathway

Observations from seismic data, horizon maps and flattening analysis indicate a relatively recent (at least from the Pliocene, 5.3 Ma) development of the graben visible at the modern seafloor (Figures 3–7, 10 and 11) and influence on the submarine channel network offshore Mafia Island.

At 15 Ma, the map of horizon M3 reveals predominantly west–east-oriented submarine channel pathways (Figure 5; Supporting Information Figure S2). Flattening analysis of the horizon M3 reveals only minimum displacements (<80 m) visible for faults located on the eastern side of the seismic line and bordering the eastern side of the graben (Figure 10c). These faults do not influence the channel pathway and are interpreted to predate the initiation of the graben. By the time of M4 deposition (5.3 Ma), a net reorganization of the slope to the deep-water drainage network is evident (Figure 6). The earlier west–east-oriented turbidite channels are disconnected and deactivated at this time (Figure 6), giving way to a new NNW–SSE channel pathway along the slope (Figures 6 and 7). The channels are structurally confined by NNW–SSE-oriented normal faults (Figures 6, 7 and 9). Flattening analysis of horizon M4 demonstrates that the initiation of the opening of the graben is consistent with the southward shift of the channels (Figure 10d). At that time, NNW–SSE-oriented normal faults dissected the western portion of the study area, thus creating a structural topographic low (graben) which funnelled the turbidite channels in a new preferred NNW–SSE-oriented pathway. This new orientation continues until the present day, as evidenced by the channel at the modern seafloor (Figures 1, 3, 4 and 7), which still follows the ramp direction of the graben border faults (Figure 7). We interpret this deformation to be coeval with the channel development, generating channel diversions.

Structures affecting the seabed and their control on the location, pathway and architecture of channel-levee systems were already observed in other studies and geological settings (Anderson et al., 2000; Broucke et al., 2004; Clark & Cartwright, 2009, 2011; Cronin, 1995; Gamboa et al., 2012; Gee & Gawthorpe, 2006, 2007; Huyghe et al., 2004; Mayall et al., 2010; Rowan & Weimer, 1998; Sinclair & Tomasso, 2002; Smith, 2004). Structurally controlled alterations of the seafloor topography result in deflection, diversion, constriction and blocking of turbidity channels (Clark & Cartwright, 2009, 2011; Gee & Gawthorpe, 2006, 2007; Mayall et al., 2010; Prather et al., 1998; Smith, 2004). In the study area, the normal downslope direction is towards the east (towards the western Indian Ocean). However, since 5.3 Ma until the present day, we observe a southward diversion of the channels away from their original route (Figures 6 and 7). The new NNW–SSE-oriented submarine channel pathway remains visible at the modern seafloor (Figure 7). It continues for ca. 50 km southward within the topographic low of the graben, until it is diverted at ca. 9° S and 40° E, where it resumes its way eastward (Figure 2a). The diversion is likely controlled by the presence of one or more fault sets oriented at a high angle to the eastwards flow direction (Clark & Cartwright, 2009; Prather et al., 1998; Sinclair & Tomasso, 2002; Smith, 2004). In this scenario, this obstacle is generated by the uplifted footwall of the eastern border of the graben that obstructs the eastward downslope flow and causes the channel to occupy the newly forming topographic low of the graben (Figures 3 and 6).

The morphology of the channels in terms of meander width and sinuosity also changed through time (Figures 5–7). We observe a net variation in channel geomorphology from relatively narrow and low sinuosity (Figure 5) during the middle Miocene (15 Ma) to wider, thicker and higher sinuosity (Figure 7) at the modern seafloor. The variability in sinuosity of turbidite channels may be generated by different factors (e.g., flow erosional component, lateral stacking, lateral accretion and seafloor topography; Mayall et al., 2006) and other external factors, including climate, sea level and tectonics (Kolla et al., 2007; Mayall et al., 2006). To understand whether this net change in channel geomorphology in the study area is due to depositional processes or is a function of changes in seafloor topography, we need to consider the relationship between deformation and sediment transport and accumulation (Howlett et al., 2020; Mayall et al., 2006) as well as changes in the slope gradient (Ferry et al., 2005; Gee & Gawthorpe, 2006; Huyghe et al., 2004). Between the middle Miocene and the Pliocene (15 to 5.3 Ma), East Africa underwent a transitional phase to cooler and drier conditions and experienced aridification towards the late Pliocene (Cerling et al., 2011; deMenocal, 2004; Levin, 2015; Uno et al., 2011). At the same time, a global sea-level highstand was recorded (Miller et al., 2020), as well as a decrease in sediment fluxes along the Tanzania margin (Dottore Stagna et al., 2022; Said et al., 2015). This phase of decreased sediment fluxes towards the western Indian Ocean and global sea level highstand agrees with a condition of reduced sediment transport-accumulation related to a period of high structural growth of the graben, as already documented in other systems (e.g., Clark & Cartwright, 2009; Gee & Gawthorpe, 2006; Howlett

et al., 2020). In fact, during this period of low sediment fluxes, sea-level highstand, drier and cooler conditions and aridification, the large diversion of the turbidite channels parallel to the structural relief occurred and was maintained over a large distance, with an increase in sinuosity (SI: 1.3) and in channel incisions (ca. 0.6 km wide and <100 m deep) (Figures 4b and 6). This phase was followed by an additional increase in channel' width and sinuosity, with the channel at the modern seafloor being wider (with the main erosional surface reaching a max width of ca. 1.5 km and a depth of 235 m), erosive and more sinuous (SI: 1.55). This more recent variation occurred during global sea level highstand (Miller et al., 2020), the passage from wooded habitats transitioned to open grasslands and more arid conditions (Bobe & Behrensmeyer, 2004) and reduced sediment fluxes (Dottore Stagna et al., 2022; Said et al., 2015).

We interpret that the structurally generated diversion of the turbidite channels (Figures 6 and 7) in smaller than two km topographic lows (Howlett et al., 2020), structural narrowing and the increase in the confinement of the channel complex (Figures 3 and 4b; Abreu et al., 2003; Kane et al., 2008), led to increase in sinuosity and widening of the channel. Although we consider the structural development of the graben and increase in confinement to be the main factors influencing the variation in morphology of the channel system, we do not exclude that sea-level highstand, arid climatic conditions, coincident with reduction in sediment fluxes and decrease in supply of coarse-grained sediments, may have promoted steadier flow (Kolla et al., 2007) and the increase in sinuosity and width of the channel (Kolla et al., 2007; Mayall et al., 2006). In addition, since 5.3 Ma the channel pathway is oriented along the slope, and a decrease in slope gradient can also generate an increase in channel sinuosity (Ferry et al., 2005; Gee & Gawthorpe, 2006; Huyghe et al., 2004; Kolla et al., 2007).

The effect of late Miocene to recent extensional tectonics on turbidity channels was observed at other locations along the Tanzanian margin (Dottore Stagna et al., 2022; Maselli et al., 2019). To the north of our study area, the asynchronous tectonic uplift and exposure above sea level of Pemba and Zanzibar islands disconnected submarine canyon-channel systems from their feeding systems (Dottore Stagna et al., 2022). This extensional regime in the northern Tanzanian margin has persisted since the middle Miocene (Dottore Stagna et al., 2022), with EARS-related normal faults dissecting pre-existing anticlines and promoting the exposure of Pemba Island as horst during the middle-late Miocene, and Zanzibar Island during the late Miocene-early Pliocene (Dottore Stagna et al., 2022). While Pemba Island was being exposed above the sea level, the graben offshore Mafia Island had not yet formed. However, the timing of a reduction in the number of deep-water channels offshore Zanzibar Island, associated with the island's uplift (Dottore Stagna et al., 2022), coincides with the opening of the graben offshore Mafia Island. Southward of our study area, Franke et al. (2015) and Maselli et al. (2019) discussed the bathymetric changes associated with the opening of the Kerimbas graben (KG) and the uplift of the Davie Ridge (DR). The KG began to open as half-graben during the Miocene and evolved into a symmetric structure since the Pliocene with the development of the eastern border fault that uplifted the DR (Franke et al., 2015; Maselli et al., 2019). This resulted in an initial reduction in turbidite channels between 15 and 5.3 Ma and a redirection of the deep-water drainage network to the north, with the DR acting as a bathymetric barrier to gravity driven-flows originating along the Tanzanian shelf-slope (Maselli et al., 2019). Consequently, this study highlights a common trend in the evolution of offshore extensional structures from north to south, not only in terms of timing and kinematics of the structures but also of their control on slope-to-deep water systems having important consequences on deep-water sediment delivery along the margin.

6.3 | Analogies between the onshore and offshore domains of the EARS

The extensional tectonic observed along the western Indian Ocean, including the newly discovered graben offshore Mafia Island, presented here, may be associated with the offshore prolongation of the EARS both in terms of kinematics and timing of its development, as supported by various studies (Dottore Stagna et al., 2022; Franke et al., 2015; Iacopini et al., 2023; Kent et al., 1971; Macgregor, 2015; Maselli et al., 2019; Mougenot et al., 1986; Nicholas et al., 2007).

The timing of formation of the graben, as well as its orientation and kinematics, is consistent with other extensional structures visible along the Tanzanian margin, thus possibly suggesting a relatively recent phase of extensional tectonics offshore, which commenced not before the middle-late Miocene (after 15 Ma). Faults at the modern seafloor, recently recorded GPS data (Stamps et al., 2021), and earthquake focal mechanisms along the Tanzania margin (Figures 2a and 9; Yang & Chen, 2010) show that tectonic activity related to the EARS is still ongoing in the area and reveal mostly W-E and SW–NE extension along the main structures offshore. This is also in agreement with our results (Figure 9) and the regional stress field (Supporting Information Figures S3 and S4; Delvaux & Barth, 2010; Craig et al., 2011; Stamps et al., 2021).

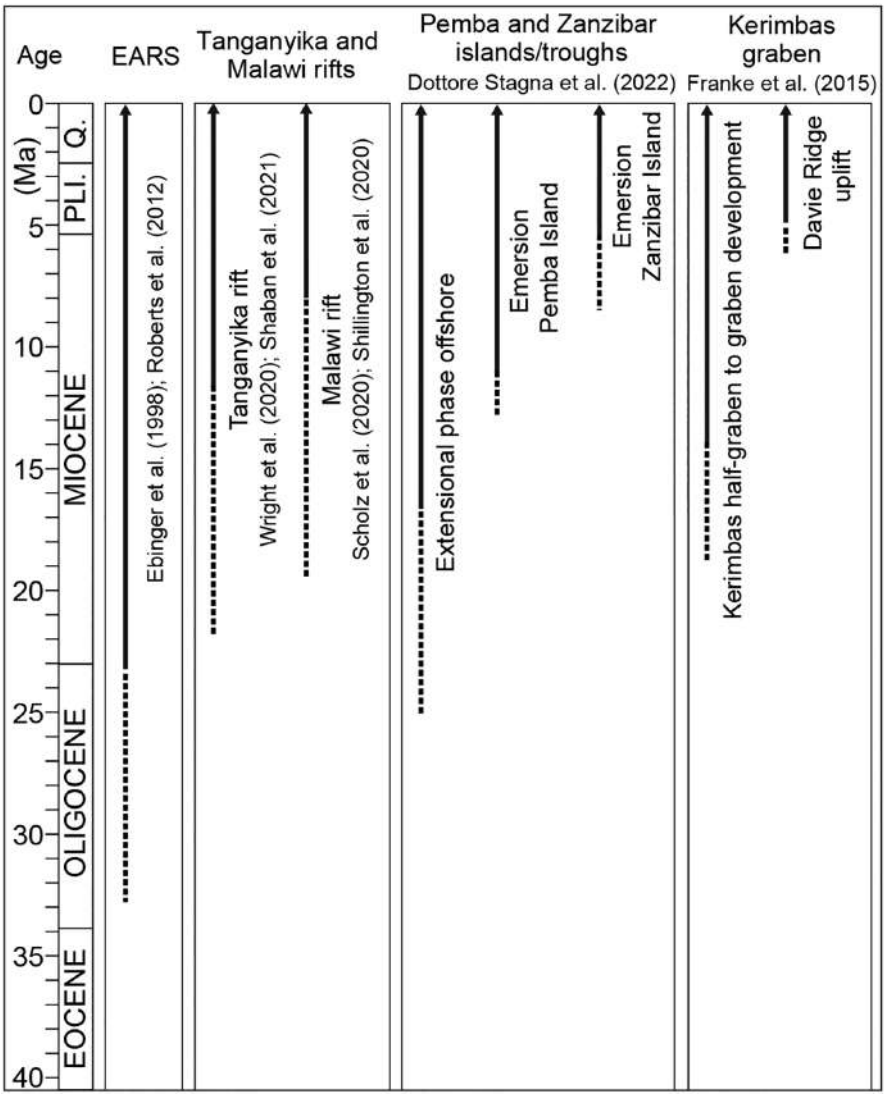

FIGURE 12 Diagram correlating the timing of regional tectonic events across different regions of the EARS (East African Rift System) and different tectonic structures, both onshore (Tanganyika and Malawi rifts) and offshore (Pemba-Zanzibar islands and Kerimbas Graben-Davie Ridge development).

Analogies between onshore and offshore rift tectonics margins can be made based on previous studies focused on the understanding of the formation of rift basins associated with the EARS (Figure 12) and their influence on the continental drainage systems (Cohen et al., 1993; Goudie, 2005; Roberts et al., 2012; Stankiewicz & de Wit, 2006), and slope-to-deep-water channel systems (Dottore Stagna et al., 2022; Maselli et al., 2019). Onshore, the palaeo-Rukwa River was flowing northwest during the Cretaceous, following the axis of northern Malawi and Rukwa Rift Basin across the present-day Tanganyika (Figure 1a), until it inverted its route flowing southward due to tilting of the Oligocene land surface associated with the onset of the African superswell (Roberts et al., 2012). Rifting and flexural uplift related to the development of the EARS' western and eastern branches generated a more 'concentrical' drainage network ca. 25 Ma (Roberts et al., 2012), whereas footwall uplift of the Tanganyika and Ubendian eastern rift flanks (Figure 1) promoted seaward directed flows in the Mio-Pliocene (Morley et al., 1990; Roberts et al., 2012). Sediment accumulation rates based on shallow cores, combined with depth to basement estimates, suggested an age of ca. 9–12 Ma for Lake Tanganyika rift initiation (Figure 12; Burgess et al., 1988; Cohen et al., 1993). However, a more recent and revisited stratigraphic framework based on syn-rift depositional sequences for this lake has been recently proposed (Muirhead et al., 2019; Shaban et al., 2021; Wright et al., 2020). The lowermost sequence ranges from mid-Miocene to early Pliocene (Macgregor, 2015; Rosendahl et al., 1988; Shaban et al., 2021), while the upper syn-rift unit (Macgregor, 2015; Rosendahl et al., 1988; Shaban et al., 2021) agrees with the basin age estimated by Cohen et al. (1993). In other words, the Tanganyika rift started opening at least since the middle Miocene (Figure 12), thus being coherent with the age of basins offshore at the same latitude (i.e. Pemba trough, Figure 1b; Dottore Stagna et al., 2022). Previous studies on the variation in depositional sequences along the border faults of the Lake Malawi rift (Figure 1;

Ebinger et al., 1984), and analysis of the basin's subsidence, thicknesses of the Cenozoic-Quaternary sedimentary sequence and elevation of the escarpments (Betzler & Ring, 1995; Flannery & Rosendahl, 1990; Specht & Rosendahl, 1989), suggested that Malawi rift started its evolution in the late Cenozoic (Figure 12). However, more recent studies estimated the onset of the extension to be at least 8.6–4.6 million years (Myr) old (Cohen et al., 1993; Ebinger et al., 1993; McCartney & Scholz, 2016; Scholz et al., 2020) and as old as 23 Myr in the

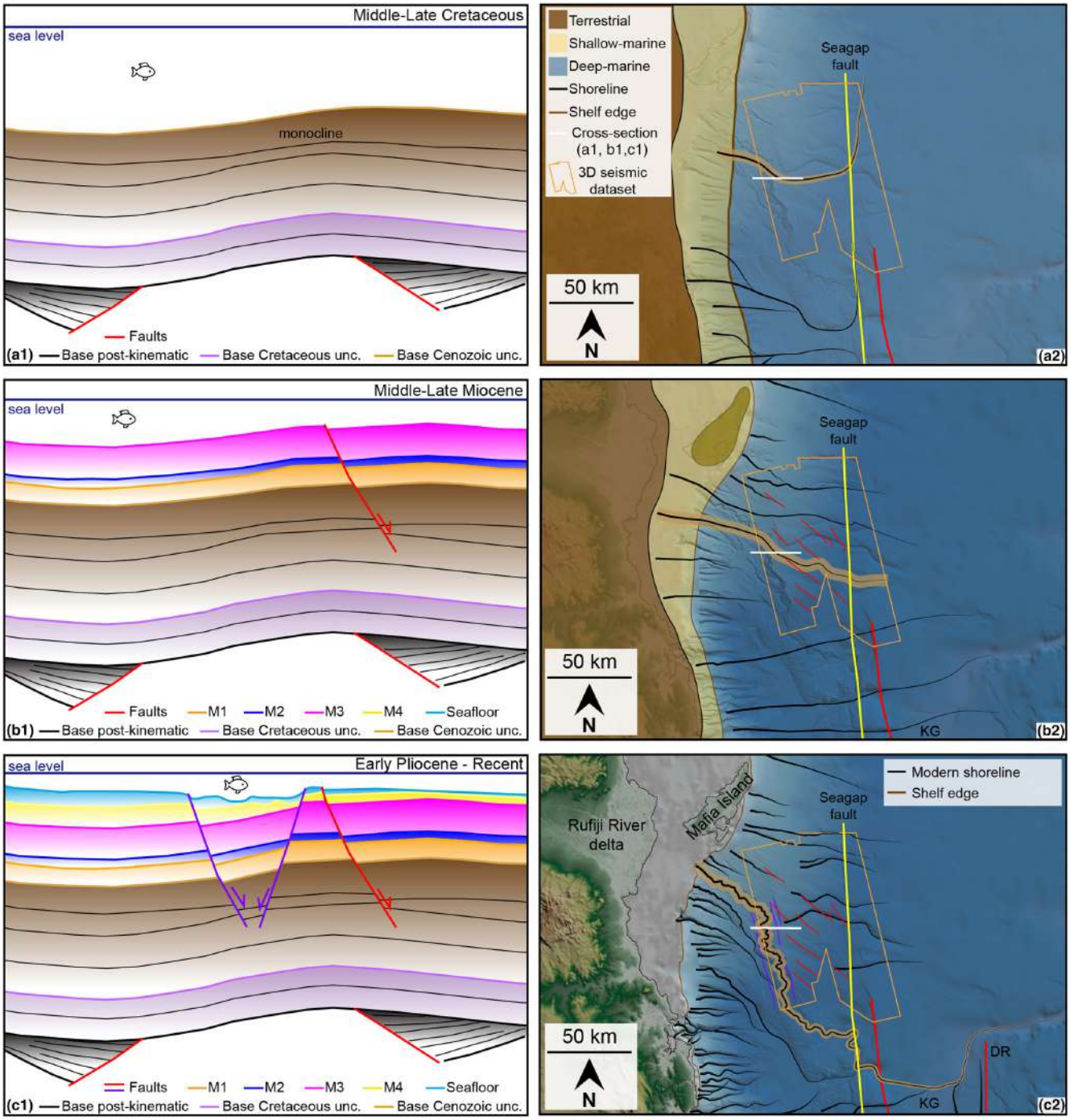

FIGURE 13 Conceptual model for the evolution of the study area from Cretaceous to present day. The model shows first the quiescent phase during the Cretaceous (Reeves, 2018), after the formation of the monocline that did not impact the W-E oriented deep-water channel network (a1, a2; see also Sansom, 2018). This quiescent phase continued until 15 Ma, with turbidite channels still mostly W-E oriented and NW-SE oriented faults being active at this time (b1, b2). The opening of the graben (ca. 5.3 Ma) completely reorganized the slope-to-deep-water channel system, redirecting southward the channel network (c1, c2). DR, Davie Ridge; KG, Kerimbas Graben.

northern portion of the Malawi rift (Mortimer et al., 2016; Roberts et al., 2012). The northern portion of the Malawi rift began forming first during the Miocene at ca. 23 Ma (Accardo et al., 2018; Betzler & Ring, 1995; Ebinger et al., 1984; Flannery & Rosendahl, 1990; Mortimer et al., 2016; Scholz et al., 2020; Shillington et al., 2020; Specht & Rosendahl, 1989) than the central southern portion, estimated to start forming maximum in the Pliocene at ca. 9 to 4 Ma (Figure 12; Ebinger et al., 1993; McCartney & Scholz, 2016; Scholz et al., 2020; Shillington et al., 2020). These results also highlight a coherent timing between onshore and offshore structures at the same latitude (graben of this study, and Kerimbas graben, Figure 1b; Franke et al., 2015; Maselli et al., 2019). However, there are still uncertainties about the timing of the extension and basin formation onshore, since the oldest syn-rift sediments were not sampled, which may mislead the understanding of the relationship between onshore and offshore structures related to the EARS. Extensional tectonic and uplifted rift shoulders also redirected the Ruaha–Rufiji and Rovuma rivers to the east (Maselli et al., 2019; Morley et al., 1992; Nicholas et al., 2007; Roberts et al., 2012; Trauth et al., 2005), with increases in sediment supply recorded offshore (Dottore Stagna et al., 2022; Said et al., 2015).

Considering what has been said about the time of rifting of Lake Tanganyika rift and Lake Malawi, we can observe a coherent timing of development offshore (Figure 12), with northern extensional structures started developing first (Pemba and Zanzibar islands and through, Figure 1b; Dottore Stagna et al., 2022), then southern extensional structures (the graben of this study and Kerimbas Graben, Figure 1b; Franke et al., 2015; Maselli et al., 2019). Extensional structures along the margin onshore and offshore rejuvenate moving southward, with the graben in our study area and KG forming as asymmetric grabens first during the Miocene (Franke et al., 2015), then as symmetric grabens only in the early Pliocene (Franke et al., 2015; Maselli et al., 2019).

6.4 | Tectonic and palaeogeographic reconstruction offshore Mafia Island

We present a palaeogeographic and tectonic model of the region from the Cretaceous to recent times that includes the development of the graben and the evolution of the slope to a deep-water channel system (Figure 13).

1. A period of tectonic quiescence in the late Cretaceous followed the reactivation of pre-existing extensional faults generating the monocline (Figure 13a1,a2). The fold did not influence the successive Cretaceous depositional processes downslope, and few onlaps are visible in the structure in between the Base Cretaceous Unconformity and the Base Cenozoic horizons (Figure 11a–d). Sansom (2018) showed that the Late Cretaceous deep-water channel system in this area flowed eastward, thus illustrating that the bathymetric deformation of the evolving monocline was not enough to stop the sediment delivery downslope.
2. A new extensional phase was established offshore starting from the Miocene and was associated with the EARS (Figure 13b1,b2). Normal faults detach from intra-Cretaceous units without affecting and decoupling from deeper structures (Figure 11).
3. The NNW–SSE graben offshore Mafia Island opened during the early Pliocene (Figure 13c1,c2), overprinting pre-existing structures and redirecting the channel network southward. This new channel pathway is still visible today (Figure 2a), with the channel flowing south changing its direction again towards the east in a more southerly position (Figure 2a).

The graben influenced, and still does, the direction of channels that have delivered sediments eastward from the African continent to the deep-water for millions of years with important consequences on the sediment delivery of more coarse-grained materials offshore.

7 | CONCLUSIONS

In this study, we reveal the presence of a previously unknown, NNW–SSE-oriented graben, located offshore Mafia Island at a water depth of ca. 1500 m below sea level, and we discuss its tectonic evolution and its impact on the submarine channel systems. Interpretation of 2D and 3D seismic reflection data combined with structural analysis shows that the formation of this extensional structure reflects the establishment of a new tectonic regime in this area since the early Pliocene (5.3 Ma) and is distinct from pre-existing Mesozoic structures. We speculate that the opening of the graben reflects a later tectonic phase of EARS that is migrating towards the offshore domain. The opening of the graben redirected southward turbidite channels trajectory from an eastward direction that was stable at least since the Cretaceous, thus deeply affecting the delivery of land-derived material to the deepsea. This modified and structurally controlled channel pathway persists today.

This study contributes to the understanding of the intricate interplay between rifted continental margin tectonics, polyphase deformation and sedimentary processes, demonstrating the ongoing impact of the EARS in the western Indian Ocean.

ACKNOWLEDGEMENTS

We are grateful to the Tanzania Petroleum Development Corporation (TPDC), WesternGeco-SLB, Shell and Shell Tanzania for giving access to the data and allowing the publication of this work. We would like to thank SLB for providing access to the deep-section of the 2D data, and academic licences of the seismic interpretation software Petrel. MDS and VM acknowledge support from Earth Sciences Doctoral Award and the Natural Sciences and Engineering Research Council of Canada (NSERC) Discovery Grant (RGPIN-2020-04461). We also thank Stefano Tavani and Cynthia Ebinger for the constructive discussions.

CONFLICT OF INTEREST STATEMENT

The authors declare that they have no conflict of interest.

DATA AVAILABILITY STATEMENT

The authors confirm that all relevant data are included in the paper. The bathymetric data presented in this study are not publicly available. All additional data are available upon reasonable request to the authors.

ORCID

Marina Dottore Stagna https://orcid.org/0000-0002-8182-0435
Vittorio Maselli https://orcid.org/0000-0001-7301-0769
David Iacopini https://orcid.org/0000-0003-4925-9665

REFERENCES

Abreu, V., Sullivan, M., Pirmez, C., & Mohrig, D. (2003). Lateral accretion packages (LAPs): An important reservoir element in deep water sinuous channels. *Marine and Petroleum Geology*, *20*, 631–648.

Accardo, N. J., Shillington, D. J., Gaherty, J. B., Scholz, C. A., Nyblade, A. A., Chindandali, P. R. N., Kamihanda, G., McCartney, T., Wood, D., & Wambura Ferdinand, R. (2018). Constraints on rift basin structure and border fault growth in the Northern Malawi rift from 3-D seismic refraction imaging. *Journal of Geophysical Research, Solid Earth*, *123*(11), 10003–10025. https://doi.org/10.1029/2018JB016504

Allmendinger, R. W. (2020). *Modern structural practice: A structural geology laboratory manual for the 21st century*. 1.9.1, 2015-2020. https://www.rickallmendinger.net/download

Ameen, M. (1988). *Folding of layered cover due to dip-slip basement faulting*. Imperial College London (University of London).

Anderson, E. M. (1905). The dynamics of faulting. *Transactions of the Edinburgh Geological Society*, *8*, 387–402.

Anderson, J. E., Cartwright, J., Drysdall, S. J., & Vivian, N. (2000). Controls on turbidite sand deposition during gravity-driven extension of a passive margin: examples from miocene sediments in block 4, Angola. *Marine and Petroleum Geology*, *17*, 1165–1203.

Bassias, Y. (1992). Petrological and geochemical investigation of rocks from the Davie fracture zone (Mozambique Channel) and some tectonic implications. *Journal of African Earth Sciences (and the Middle East)*, *15*(3–4), 321–3311.

Beloussov, V. V. (1959). Types of fodling and their origin. *International Geology Review*, *2*, 1–21.

Betzler, C., & Ring, U. (1995). Sedimentology of the Malawi rift: Facies and stratigraphy of the Chiwondo beds, northern Malawi. *Journal ofHuman Evolution*, *28*(1), 23–35.

Bland, S., Griffiths, P., & Hodge, D. (2004). Restoring the seismic image with a geological rule base. *First Break*, *22*, 51–55.

Bobe, R., & Behrensmeyer, A. K. (2004). The expansion of grassland ecosystems in Africa in relation to mammalian evolution and the origin of the genus Homo. *Palaeogeography, Palaeoclimatology, Palaeoecology*, *207*, 399–420.

Broucke, O., Temple, F., Rouby, D., Robin, C., Calassou, S., Nalpas, T., & Guillocheau, F. (2004). The role of deformation processes on the geometry of mud-dominated turbiditic systems, oligocene and lower-middle Miocene of the lower Congo Basin (West African margin). *Marine and Petroleum Geology*, *21*, 327–348.

Buitner, S. (2014). How plumes help to break plates. *Nature*, *513*, 36–37. https://doi.org/10.1038/513036a

Bull, S., Browne, G. H., Arnot, M. J., & Strachan, L. J. (2020). Influence of mass transport deposits (MTD) surface topography on deep-water deposition: An example from predominantly fine -grained continental margin, New Zealand. *Geological Society, London, Special Publication*, *500*, 147–171. https://doi.org/10.1144/SP500-2019-192

Burgess, C. F., Rosendahl, B. R., Sander, S., Burgess, C. A., Lambiase, J., Derksen, S., & Meader, N. (1988). Chapter 35—The structural and stratigraphic evolution of Lake Tan-ganyika: A case study of continental rifting. *Developments in Geotectonics*, *22*, 859–881. https://doi.org/10.1016/B978-0-444-42903-2.50040-3

Burke, K. (1996). The African Plate. *South Africa Journal Geology*, *99*, 339–409. https://doi.org/10.10520/EJC-942801f20

Carter, L., Burnett, D., Drew, S., Hagadorn, L., Marle, G., Bartlett-McNeil, D., & Irvin, N. (2009). *Submarine cables and the oceans: Connecting the world* No. 31 The United Nations Environment Programme World Conservation Monitoring Centre Biodiversity Series (p. 64). ICPC/UNEP/UNEP-WCMC. http://www.iscpc.org/publications/ICPC-UNEP_Report.pdf

Carter, L., Milliman, P. J., Talling, R., Gavey, R., & Wynn, R. B. (2012). Near-synchronous and delayed initiation of long run-out submarine sediment flows from a record-breaking river flood, offshore Taiwan. *Geophysical Research Letters*, *39*, L12603. https://doi.org/10.1029/2012GL051172

Cerling, T. E., Wynn, J. G., Andanje, S. A., Bird, M. I., Korir, D. K., Levin, N. E., Mace, W., Macharia, A. N., Quade, J., & Remien, C. H. (2011). Woody cover and hominin environments in the past 6 million years. *Nature*, *476*, 51–56.

Chen, Q., & Sidney, S. (1997). Seismic attribute technology for reservoir forecasting and monitoring. *The Leading Edge*, *16*, 445–448. https://doi.org/10.1190/1.1437657

Chopra, S., & Marfurt, K. J. (2007). Seismic attributes for prospect identification and reservoir characterization. *Society of Exploration Geophysicists, Geophysical Developments*, *11*, 481. https://doi.org/10.1190/1.9781560801900

Clark, I. R., & Cartwright, J. A. (2009). Interactions between submarine channel systems and deformation in deepwater fold belts: Examples from the Levant Basin, Eastern Mediterranean sea. *Marine and Petroleum Geology*, *26*, 1465–1482.

Clark, I. R., & Cartwright, J. A. (2011). Key controls on submarine channel development in structurally active settings. *Marine and Petroleum Geology*, *28*(7), 1333–1349.

Coffin, M. F., & Rabinowitz, P. D. (1992). The Mesozoic east African and Madagascan conjugate continental margins stratigraphy and tectonics. In J. S. Watkins, Z. Feng, & K. J. McMillen (Eds.), *Geology and geophysics of continental margins* (pp. 2011–2240). AAPG Memoir 53.

Cohen, A. S., Soreghan, M. J., & Scholz, C. A. (1993). Estimating the age of formation of lakes: An example of Lake Tanganyika, East African Rift System. *Geology*, *21*, 511–514.

Cohen, H. A., & McClay, K. (1996). Sedimentation and shale tectonics of the northwestern Niger Delta front. *Marine and Petroleum Geology*, *13*(3), 313–328.

Covault, J. A., Fildani, A., Romans, B. W., & McHargue, T. (2011). The natural range of submarine canyon-and-channel longitudinal profiles. *Geosphere*, *7*(2), 313–332.

Covault, J. A., Shelef, E., Traer, M., Hubbard, S. M., Romans, B. W., & Fildani, A. (2012). Deep-water channel run-out length: Insights from seafloor geomorphology. *Journal of Sedimentary Research*, *82*(1), 25–40.

Craig, T. J., Jackson, J. A., Priestley, K., & McKenzie, D. (2011). Earthquake distribution patterns in Africa: Their relationship to variations in lithospheric and geological structure, and their rheological implications. *Geophysical Journal International*, *185*(1), 403–434.

Cronin, B. T. (1995). Structurally-controlled deep sea channel courses: Examples from the miocene of Southeast Spain and the Alboran Sea, Southwest Mediterranean. *Geological Society, London, Special Publications*, *94*, 115–135.

Delaunay, B. (1934). Sur la sphère vide. A la mémoire de Georges Voronoi. *Izvestiya Akademii Nauk SSSR, Otdelenie Matematicheskih i Estestvennyh Nauk*, *7*, 793800.

Delvaux, D., & Barth, A. (2010). African stress pattern from formal inversion of focal mechanism data. *Tectonophysics*, *482*(1–4), 105–128.

deMenocal, P. B. (2004). African climate change and faunal evolution during the Pliocene-Pleistocene. *Earth and Planetary Science Letters, Frontiers*, *220*, 3–24.

Deptuck, M. E., Sylvester, Z., Pirmez, C., & O'Byrne, C. (2007). Migration-aggradation history and 3-D seismic geomorphology of submarine channels in the Pleistocene Benin-major Canyon, western Niger Delta slope. *Marine and Petroleum Geology*, *24*, 406–433. https://doi.org/10.1016/j.marpetgeo.2007.01.005

Dottore Stagna, M., Maselli, V., Grujic, D., Reynolds, P., Reynolds, D., Iacopini, D., Richards, B., Underhill, J. R., & Kroon, D. (2022). Structural controls on slope evolution and sediment dispersal pathways along the northern Tanzania continental margin, western Indian Ocean. *Marine Geology*, *443*, 106662. https://doi.org/10.1016/j.margeo.2021.106662

Dottore Stagna, M., Maselli, V., & van Vliet, A. (2023). Large-scale submarine landslide drives long-lasting regime shift in slope sediment deposition. *Geology*, *51*(2), 167–173. https://doi.org/10.1130/G50463.1

Ebinger, C. J., Crow, M. J., Rosendahl, B. R., Livingstone, D. A., & LeFournier, J. (1984). Structural evolution of Lake Malawi, Africa. *Nature*, *308*, 627–629.

Ebinger, C. J., Deino, A. L., Tesha, A. L., Becker, T., & Ring, U. (1993). Tectonic controls on rift basin morphology evolution of the Northern Malawi (Nyasa) Rift. *Journal of Geo-Physical Research: Solid Earth*, *98*(B10), 17821–17836.

Ebinger, C. J., Reiss, M. C., Bastow, I., & Karanja, M. M. (2024). Shallow sources of upper mantle seismic anisotropy in East Africa. *Earth and Planetary Science Letters*, *625*, 118488.

Ebinger, C. J., & Sleep, N. (1998). Cenozoic magmatism throughout East Africa resulting from impact of a single plume. *Nature*, *395*, 788–791. https://doi.org/10.1038/27417

Ekstrom, G., Nettles, M., & Dziewonski, A. M. (2012). The global CMT project 2004–2010:Centroid-moment tensors for 13,017 earthquakes. *Physics of the Earth and Planetary Interiors*, *200–201*, 1–9.

Erslev, E. A. (1991). Trishear Fault-Propagation Folding. *Geolofy*, *19*(6), 617–620. https://doi.org/10.1130/0091-7613(1991)019<0617:TFPF>2.3.CO;2

Fernandes, R. M. S., Miranda, J. M., Delvaux, D., Stamps, D. S., & Saria, E. (2013). Re-evaluation of the kinematics of Victoria Block using continuous GNSS data. *Geophysics Journal International*, *193*, 1–10. https://doi.org/10.1093/gji/ggs071

Ferrill, D. A., Morris, A. P., & McGinnis, R. N. (2012). Extensional fault propagation folding in mechanically layered rocks: The case against the frictional drag mechanism. *Tectonophysics*, *576*, 78–85. https://doi.org/10.1016/j.tecto.2012.05.023

Ferrill, D. A., Morris, A. P., & Smart, K. J. (2007). Stratigraphic control on extensional fault propagation folding: Big Brushy Canyon monocline, Sierra Del Carmen, Texas. *Geological Society, London, Special Publications*, *292*, 203–217. https://doi.org/10.1144/SP292.12

Ferry, J. N., Mulder, T., Parize, O., & Raillard, S. (2005). Concept of equilibrium profile in deep-water turbidite systems: Effects of local physiographic changes on the nature of sedimentary process and the geometries of deposits. *Geological Society of London, Special Publication London*, *244*(1), 181–193.

Flannery, J., & Rosendahl, B. (1990). The seismic stratigraphy of Lake Malawi, Africa: Implications for interpreting geological processes in lacustrine rifts. *Journal of African Earth Sciences (and the Middle East)*, *10*(3), 519–548.

Franke, D., Jokat, W., Ladage, S., Stollhofen, H., Klimke, J., Lutz, R., Mahanjane, E. S., Ehrhardt, A., & Schreckenberger, B. (2015). The offshore East African Rift System: Structural framework at the toe of a juvenile rift. *Tectonics*, *34*, 2086–2104. https://doi.org/10.1002/2015TC003922

Fuhrmann, A., Kane, I. A., Clare, M. A., Ferguson, R. A., Schomacker, E., Bonamini, E., & Contreras, F. A. (2020). Hybrid turbidite-drift channel complexes: An integrated multiscale model. *Geology*, *48*, 562–568. https://doi.org/10.1130/G47179.1

Gamboa, D., Alves, T. M., & Cartwright, J. (2012). A submarine channel confluence classification for topographically confined slopes. *Marine and Petroleum Geology*, *35*, 176–189.

Gawthorpe, R. L., Jackson, C. A.-L., Young, M. J., Sharp, I. R., Moustafa, A. R., & Leppard, C. W. (2003). Normal fault growth, displacement localisation and the evolution of normal fault populations: The Hammam Faraun fault block, Suez Rift, Egypt. *Journal of Structural Geology*, *25*, 883–895. https://doi.org/10.1016/S0191-8141(02)00088-3

Gawthorpe, R. L., Sharp, I., Underhill, J. R., & Gupta, S. (1997). Linked sequence stratigraphic and structural evolution of propagating normal faults. *Geology*, *25*, 795–798. https://doi.org/10.1130/0091-7613(1997)025<0795:LSSASE>2.3.CO;2

Gee, M., & Gawthorpe, R. L. (2006). Submarine channel controlled by salt tectonics: Examples from 3D seismic data offshore Angola. *Marine and Petroleum Geology*, *23*, 443–458.

Gee, M., & Gawthorpe, R. L. (2007). Early evolution of submarine channels offshore Angola revealed by three-dimensional seismic data. *Geological Society, London, Special Publications*, *277*, 223–235.

Goudie, A. S. (2005). The drainage of Africa since Cretaceous. *Geomorphology*, *67*(3), 437–456. https://doi.org/10.1016/j.geomorph.2004.11.008

Gunter, W., Bachu, S., & Benson, S. (2004). The role of hydrogeological and geochemical trapping in sedimentary basins for secure geological storage of carbon dioxide. *Geological Society, London, Special Publications*, *233*, 129–145.

Hardy, S., & Finch, E. (2006). Discrete element modelling of the influence of cover strength on basement-involved fault-propagation folding. *Tectonophysics*, *415*, 225–238. https://doi.org/10.1016/j.tecto.2006.01.002

Hardy, S., & McClay, K. (1999). Kinematic modelling of extensional fault-propagation folding. *Journal of Structural Geology*, *21*, 695–702.

Heijnen, M. S., Clare, M. A., Cartigny, M. J. B., Talling, P. J., Hage, S., Pope, E. L., Bailey, L., Sumner, E., Lintern, D. G., Stacey, C., Parsons, D. R., Simmons, S. M., Chen, Y., Hubbard, S. M., Eggenhuisen, J. T., Kane, I., & Hughes Clarke, J. E. (2022). Fill, flush or shuffle: How is sediment carried through submarine channels to build lobes? *Earth and Planetary Science Letters*, *584*, 117481.

Heirtzler, J. R., & Burroughs, R. H. (1971). Madagascar's paleoposition: New data from the Mozambique Channel. *Science*, *174*, 488–490. https://doi.org/10.1126/science.174.4008.488

Howlett, D. M., Gawthorpe, R. L., Ge, Z., Rotevatn, A., & Jackson, C.A.-L. (2020). Turbidites, topography and tectonics: Evolution of submarine channel-lobe systems in the salt-influenced Kwanza Basin, offshore Angola. *Basin Research*, *33*(2), 1076–1110.

Hudson, F. S. (1955). Folding of unmetamorphosed strata superjacent to massive basement rocks. *Bulletin of the American Association of Petroleum Geologists*, *39*, 2038–2051.

Huyghe, P., Foata, M., Deville, E., & Mascle, G. (2004). Channel profiles through the active thrust front of the southern Barbados prism. *Geology*, *32*, 429–432.

Iacopini, D., Tavani, S., Pentagallo, S., Maselli, V., Dottore Stagna, M., Ebinger, C. J., Reynolds, D., & van Vliet, A. (2023). Architecture, structural and tectonic significance of the Seagap fault (offshore Tanzania) in the framework of the East African Rift. *Basin Research*, *35*(1), 387–412. https://doi.org/10.1111/bre.12716

Jackson, C. A.-L., Gawthorpe, R. L., & Sharp, I. R. (2006). Style and sequence of deformation during extensional fault-propagation folding: Examples from the Hammam Faraun and El-Qaa fault blocks, Suez Rift, Egypt. *Journal of Structural Geology*, *28*, 519–535. https://doi.org/10.1016/j.jsg.2005.11.009

Janecke, S. U., Vanderburg, C. J., & Blankenau, J. J. (1998). Geometry, mechanism, and significance of extensional folds from examples in the Rocky Mountain Basin and Range province, U.S.A. *Journal of Structural Geology*, *20*, 841–856. https://doi.org/10.1016/S0191-8141(98)00016-9

Jokat, W., Altenbernd, T., Eagles, G., & Geissler, W. H. (2021). The early drift of the Indian plate. *Scientific Reports*, *11*(1), 10796.

Kane, I. A., McCaffrey, W. D., & Peakall, J. (2008). Controls on sinuosity evolution within submarine channels. *Geology*, *36*, 287–290.

Keller, J. V. A., & Lynch, G. (1999). Displacement transfer and forced folding in the Maritimes basin of Nova Scotia, eastern Canada. *Geological Society of London, Special Publication*, *169*, 87–101. https://doi.org/10.1144/GSL.SP.2000.169.01.07

Kent, P. E., Hunt, J. A., & Johnstone, D. W. (1971). The geology and geophysics of coastal Tanzania. *Institute of Geological Sciences (UK) Geophysical*, *6*, 101 p.

Khalil, S. M., & McClay, K. R. (2002). Extensional fault-related folding, northwestern Red Sea, Egypt. *Journal of Structural Geology*, *24*, 743–762.

Klimke, J., & Franke, D. (2016). Gondwana breakup: No evidence for a Davie fracture zone offshore northern Mozambique. *Tanzania and Kenya. Terra Nova*, *210*(4), 233–244. https://doi.org/10.1111/ter.12214

Kneller, B., Dykstra, M., Fairweather, L., & Milana, J. P. (2016). Mass-transport and slope accommodation: Implications for turbidite sandstone reservoir. *American Association of Petroleum Geologists Bulletin*, *100*, 213–235. https://doi.org/10.1306/09011514210

Kolla, V., Kostecki, J. A., Henderson, L., & Hess, L. (1980). Morphology and quaternary sedimentation of the Mozambique fan and environs, southwestern Indian Oceans. *Sedimentology*, *27*, 357–378.

Kolla, V., Posamentier, H. W., & Wood, L. J. (2007). Deep-water and fluvial sinuous channels—Characteristics, similarities and dissimilarities, and modes of formation. *Marine and Petroleum Geology*, *24*, 388–405.

Levin, N. E. (2015). Environment and climate of early human evolution. *Annual Review Earth and Planetary Sciences*, *43*, 405–429.

Macgregor, D. (2015). History of the development of the East African Rift System: A series of interpreted maps through time. *Journal of African Earth Sciences*, *101*, 232–252. https://doi.org/10.1016/j.jafrearsci.2014.09.016

Mahanjane, E. S. (2014). The Davie fracture zone and adjacent basins in the offshore Mozambique margin—A new insights for the hydrocarbon potential. *Marine and Petroleum Geology*, *57*, 561–571. https://doi.org/10.1016/j.marpetgeo.2014.06.015

Martínez-Doñate, A., Privat, A., Hodgson, D. M., Jackson, C., Kane, I. A., Spychala, Y. T., Duller, R. A., Stevenson, C., Keavney, E., Schwarz, E., & Flint, S. (2021). Substrate entrainment, depositional relief, and sediment capture: Impact of a submarine landslide on flow process and sediment supply. *Frontiers in Earth Science*, *9*, 757617, https://doi.org/10.3389/feart.2021.757617

Maselli, V., Iacopini, D., Ebinger, C. J., Tewari, S., de Haas, H., Wade, B. S., Pearson, P. N., Francis, M., van Vliet, A., Richards, B., & Kroon, D. (2020). Large-scale mass wasting in the western Indian Ocean constrains onset of East African rifting. *Nature Communications*, *11*, 3456. https://doi.org/10.1038/s41467-020-17267-5

Maselli, V., Kroon, D., Iacopini, D., Wade, B. S., Pearson, P. N., & de Haas, H. (2019). Impact of the East African Rift System on the routing of the deep-water drainage network offshore Tanzania, western Indian Ocean. *Basin Research*, *32*, 1–15. https://doi.org/10.1111/bre.12398

Mayall, M., Jones, E., & Casey, M. (2006). Turbidite channel reservoirs—Key elements in facies prediction and effective development. *Marine and Petroleum Geology*, *23*(8), 821–841.

Mayall, M., Lonergan, L., Bowmn, A., James, S., Milles, K., Primmer, T., Pope, D., Rogers, L., & Skeene, R. (2010). The response of turbidite slope channels to growth induced seabed topography.

American Association of Petroleum Geologists Bulletin, *94*, 1011–1030.

McCartney, T., & Scholz, C. A. (2016). A 1.3-million-year record of synchronous faulting in the hangingwall and border fault of a half-graben inthe Malawi (Nyasa) Rift. *Journal of Structural Geology*, *91*, 114–129. https://doi.org/10.1016/j.jsg.2016.08.012

Miller, K. G., Browning, J. V., Schmelz, W. J., Kopp, R. E., Mountain, G. S., & Wright, J. D. (2020). Cenozoic Sea-level and cryospheric evolution from deep-sea geochemical and continental margin records. Science. *Advances*, *6*(20), eaaz1346.

Mitchum Jr., R. M., Vail, P. R., & Sangree, J. B. (1977). Seismic stratigraphy and global changes of sea level, part 6: Seismic stratigraphy interpretation of seismic reflection patterns in depositional sequence. C.E. Payton (Ed.), *Seismic stratigraphy—Applications to hydrocarbon exploration* (Vol. *25*, pp. 117–133). AAPG Memoir.

Morley, C. K., Nelson, R. A., Patton, T. L., & Munn, S. G. (1990). Transfer zones in the east African Rift system and their relevance to hydrocarbon exploration in rifts. *American Association of Petroleum Geologists Bulletin*, *74*, 1234–1253.

Morley, C. K., Wescott, W. A., Stone, D. M., Harper, R. M., Wigger, S. T., & Karanja, F. M. (1992). Tectonic evolution of the northern Kenyan Rift. *Journal of Geological Society*, *149*, 333–348. https://doi.org/10.1144/gsjgs.149.3.0333

Mortimer, E., Kirstein, L. A., Stuart, F. M., & Strecker, M. R. (2016). Spatio-temporal trends in normal-fault segmentation recorded by low-temperature thermochronology: Livingstone fault scarp, Malawi Rift, East African Rift System. *Earth and Planetary Science Letters*, *455*, 62–72. https://doi.org/10.1016/j.epsl.2016.08.040

Mougenot, D., Recq, M., Virlogeux, P., & Lepvrier, C. (1986). Seaward extension of the East African Rift. *Nature*, *321*, 599–603. https://doi.org/10.1038/321599a0

Muirhead, J. D., Wright, L. J. M., & Scholz, C. A. (2019). Rift evolution in regions of low magma input in East Africa. *Earth and Planetary Science Letters*, *506*, 332–346. https://doi.org/10.1016/j.epsl.2018.11.004

Mutti, E., Bernoulli, F. R., Lucchi, F. R., & Tinterri, R. (2009). Turbidites and turbidity currents from Alpine 'flysch' to the exploration of continental margins. *Sedimentology*, *56*, 267–318.

Nicholas, C. J., Pearson, P. N., McMillan, I. K., Ditchfield, P. W., & Singano, J. M. (2007). Structural evolution of southern coastal Tanzania since the Jurassic. *Journal of African Earth Sciences*, *48*, 273–297.

Pascoe, R., Hooper, R., Storhaug, K., & Harper, H. (1999). Evolution of extensional styles at the southern termination of the Nordland Ridge, mid-Norway: A response to variations in coupling above Triassic salt. *Geological Society, London, Petroleum Geology Conference Series*, *5*, 83–90.

Patton, T. L. (1984). *Normal faulting and fold development in sedimentary rocks above a pre-existing basement normal fault* (PhD thesis). Texas A&M University.

Phethean, J. J. J., Kalnins, L. M., van Hunen, J., Biffi, P. G., Davies, R. J., & McCaffrey, K. J. W. (2016). Madagascar's escape from Africa: A high- resolution plate reconstruction for the Western Somali Basin and implications for supercontinent dis-persal. *Geochemistry, Geophysics, Geosystems*, *111*, 5036–5055. https://doi.org/10.1002/2016GC006624

Pigott, J., Kang, M.-H., & Han, H.-C. (2013). First order seismic attributes for clastic seismic facies interpretation: Examples from the East China Sea. *Journal of Asian Earth Sciences*, *66*, 34–54. ISSN 1367-9120. https://doi.org/10.1016/j.jseaes.2012.11.043

Piper, D. J. W., Cochonat, P., & Morrison, M. (1999). The sequence of events around the epicentre of the 1929 Grand Banks earthquake: Initiation of debris flows and turbidity currents inferred from sidescan sonar. *Sedimentology*, *46*, 79–97.

Piper, D. J. W., & Normark, W. R. (2001). Sandy fans-from Amazon to Hueneme and beyond. *American Association of Petroleum Geology AAPG Bulletin*, *85*(8), 1407–1438.

Piper, D. J. W., & Normark, W. R. (2009). Processes that initiate turbidity currents and their influence on turbidites: A marine geology perspective. *Journal of Sedimentary Research*, *79*, 347–362.

Posamentier, H. W., & Kolla, V. (2003). Seismic geomorphology and stratigraphy of depositional elements in deep-water settings. *Journal of Sedimentary Research*, *73*, 367–388. https://doi.org/10.1306/111302730367

Prather, B. E., Booth, J. R., Steffens, G. S., & Craig, P. A. (1998). Classification, lithologic calibration and stratigraphic succession of seismic facies from intraslope Basins, Deep Water Gulf of Mexico, USA. *AAPG Bulletin*, *82*(5), 701–728.

Prucha, J. J., Graham, J. A., & Nickelsen, R. P. (1965). Basement-controlled deformation in Wyoming Province of Rocky Mountains foreland. *Bulletin of the American Association of Petroleum Geologists*, *49*, 966–992.

Qin, Y. P., Alves, T. M., Constantine, J., & Gamboa, D. (2017). The role of mass wasting in the progressive development of submarine channels (Espírito Santo Basin, SE Brazil). *Journal of Sedimentary Research*, *87*, 500–516. https://doi.org/10.2110/jsr.2017.18

Reeves, C. V. (2018). The development of the East African margin during Jurassic and Lower Cretaceous times: A perspective from global tectonics. *Petroleum Geoscience*, *24*, 41–56.

Reeves, C. V., Teasdale, J. P., & Mahanjane, E. S. (2016). Insight into the eastern margin of Africa from a new tectonic model of the Indian Ocean. *Geological Society, London, Special Publications*, *431*, 299–322. https://doi.org/10.1144/SP431.12

Roberts, E. M., Stevens, N. J., O'Connor, P. M., Dirks, P. H. G. M., Gottfried, M. D., Clyde, W. C., & Hemming, S. (2012). Initiation of the western branch of the East African Rift coeval with the eastern branch. *Nature Geoscience*, *5*, 289–294. https://doi.org/10.1038/ngeo1432

Roche, V., & Ringenbach, J. C. (2022). The Davie fracture zone: A recorder of continents drifts and kinematic changes. *Tectonophysics*, *823*, 229188. ISSN 0040-1951. https://doi.org/10.1016/j.tecto.2021.229188

Rosendahl, B. R., Scholz, C. A., & Woods, L. D. (1988). *Seismic Atlas of Lake Tanganyika. Project PROBE* (p. 81). Duke University.

Rouby, D., Fossen, H., & Cobbold, P. R. (1996). Extension, displacement, and block rotation in the larger Gullfaks area, northern North Sea: Determined from map view restoration. *Bulletin of the American Association of Petroleum Geologists*, *80*(6), 875–889.

Rouby, D., Xiao, H., & Suppe, J. (2000). 3-D restoration of complexly folded and faulted surfaces using multiple unfolding mechanisms. *Bulletin of the American Association of Petroleum Geologists*, *84*(6), 805–829.

Rowan, M. G., & Weimer, P. (1998). Salt-sediment interaction, northern Green canyon and Ewing Bank (offshore Louisiana), northern Gulf of Mexico. *AAPG Bulletin*, *82*, 1055–1082.

Said, A., Moder, C., Clark, S., & Abdelmalak, M. M. (2015). Sedimentary budgets of the Tanzania coastal basin and implications for uplift history of the East African rift system. *Journal of African Earth Sciences*, *111*, 288–295. https://doi.org/10.1016/j.jafrearsci.2015.08.012

Sandford, A. R. (1959). Analytical and experimental study of simple geological structures. *Geological Society of America Bulletin*, *70*, 19–52.

Sansom, P. (2018). Hybrid turbidite-contourite systems of the Tanzanian margin. *Petroleum Geoscience*, *24*, 258–276. https://doi.org/10.1144/petgeo2018-044

Saria, E., Calais, E., Delvaux, D., Hartnady, C. J. H., & Stamps, D. S. (2014). Present-day kinematics of the east African rift. *Journal of Geophysical Research. Solid Earth*, *1111*, 3584–3600. https://doi.org/10.1002/2013JB0101101

Sauter, D., Ringenbach, J. C., Cannat, M., Maurin, T., Manatschal, G., & McDermott, K. G. (2018). Intraplate deformation of oceanic crust in the West Somali Basin: Insights from long-offset reflection seismic data. *Tectonics*, *37*(2), 588–603. https://doi.org/10.1002/2017TC004700

Scarselli, N. (2022). Exploring the predictive power of seismic geomorphology to assess sedimentary characteristics of gravity-flow deposits: Examples from offshore East and West Africa reservoirs. *Geological Society, London, Special Publications*, *525*, 163–188. https://doi.org/10.1144/SP525-2021-58

Schlische, R. W. (1995). Geometry and origin of fault-related folds in extensional settings. *American Association of Petroleum Geology AAPG Bulletin*, *79*, 1661–1678. https://doi.org/10.1306/7834DE4A-1721-11D7-8645000102C1865D

Scholz, C. A., Shillington, D. J., Wright, L. J. M., Accardo, N., Gaherty, J. B., & Chindandali, P. (2020). Intrarift fault fabric, segmentation,and basin evolution of the Lake Malawi (Nyasa) Rift, East Africa. *Geosphere*, *16*(5), 1293–1311. https://doi.org/10.1130/GES02228.1

Scrutton, R. A. (1978). Davie fracture zone and the movement of Madagascar. *Earth and Planetary Science Letters*, *311*(1), 104–1010. https://doi.org/10.1016/0012-1021X(1110)110143-11

Shaban, S. N., Scholz, C. A., Muirhead, J. D., & Wood, D. A. (2021). The stratigraphic evolution of the Lake Tanganyika Rift, East Africa: Facies distributions and paleo-environmental implications. *Paleogeography, Paleoclimatology, Palaeoecology*, *575*, 110474. https://doi.org/10.1016/j.palaeo.2021.110474

Shepard, F. P. (1936). The underlying causes of submarine canyons. *National Academy of Sciences of the USA*, *22*, 496–502. https://doi.org/10.1073/pnas.22.8.496

Shillington, D. J., Scholz, C. A., Chindandali, P. R. N., Gaherty, J. B., Accardo, N. J., Onyango, E., Ebinger, C., & Nyblade, A. A. (2020). Controls on intrarift faultingin the North Basin of the Malawi (Nyasa) Rift, East Africa. *Tectonics*, *39*, e2019TC005633. https://doi.org/10.1029/2019TC005633

Sii, P., & Underhill, J. R. (2015). Role of punctuated subsidence and structural inversion in creating the East African Spice Islands. In *77th EAGE Conference and Exhibition 2015*, 2015, 1–5.

Sinclair, H. R., & Tomasso, M. (2002). Depositional evolution of confined Turbidite Basins. *Journal of Sedimentary Research*, *72*, 451–456.

Sinha, S. T., Saha, S., Longacre, M., Basu, S., Jha, R., & Mondal, T. (2019). Crustal architecture and nature of continental breakup along a transform margin: New insights from Tanzania–Mozambique margin. *Tectonics*, *38*(4), 20110TC005221. https://doi.org/10.10211/20110TC005221

Smith, R. (2004). Silled sub-Basins to connected tortuous corridors: Sediment distribution systems on topographically complex sub-aqueous slopes. *Geological Society, London, Special Publications*, *222*(1), 23–44.

Specht, T. D., & Rosendahl, B. R. (1989). Architecture of the Lake Malawi Rift, East Africa. *Journal of African Earth Sciences*, *8*, 355–382. https://doi.org/10.1016/S0899-5362(89)80032-6

Stamps, D., Calais, E., Saria, E., Hartnady, C., Nocquet, J., Ebinger, C. J., & Fernandez, R. (2008). A kinematic model for the east African rift. *Geophysical Research Letters*, *119*(6), L05304. https://doi.org/10.10211/20011GL03211101

Stamps, D., Saria, E., & Kreemer, C. (2018). A geodetic strain rate model for the east African rift system. *Scientific Reports*, *8*, 732. https://doi.org/10.1038/s41598-017-19097-w

Stamps, D. S., Kreemer, C., Fernandes, R., Rajaonarison, T. A., & Rambolamanana, G. (2021). Redefining East African Rift system kinematics. *Geology*, *49*(2), 150–155.

Stankiewicz, J., & de Wit, M. J. (2006). A proposed drainage evolution model for Central Africa—Did The Congo flow east? *Journal of African Earth Sciences*, *44*(1), 75–84.

Stearns, D. W. (1978). Faulting and forced folding in the Rocky Mountain foreland, in: Laramide folding associated with basement block faulting in the Western United States. *Geological Society of America Memoir*, *151*, 1–37. https://doi.org/10.1130/MEM151-p1

Suppe, J., & Medwedeff, D. A. (1984). Fault-propagation folding. *Geological Society of American*, *16*, 670.

Talling, P. J., Allin, J., Armitage, D. A., Arnott, R. W. C., Cartigny, M. J. B., Clare, M. A., & Felletti, F. (2015). Key future directions for research on turbidity currents and their deposits. *Journal of Sedimentary Research*, *85*(2), 153–169.

Talling, P. J., Baker, M. L., Pope, E. L., Ruffell, S. C., Jacinto, R. S., Heijnen, M. S., Hage, S., Simmons, S. M., Hasenhündl, M., Heerema, C. J., McGhee, C., Apprioual, R., Ferrant, A., Cartigny, M. J. B., Parsons, D. R., Clare, M. A., Tshimanga, R. M., Trigg, M. A., Cula, C. A., … Hilton, R. J. (2022). Longest sediment flows yet measured show how major rivers connect efficiently to deep sea. *Nature Communications*, *13*, 4193.

Talling, P. J., Hage, S., Baker, M. L., Bianchi, T. S., Hilton, R. G., & Maier, K. L. (2023). The global turbidity current pump and its implications for organic carbon cycling. *Annual Review of Marine Science*, *16*, 105–133.

Talling, P. J., Wynn, R. B., Masson, D. G., Frenz, M., Cronin, B. T., Schiebel, R., Akhmetzhanov, A. M., Dallmeier-Tiessen, S., Benetti, S., Weaver, P. P. E., Georgiopoulou, A., Zühlsdorff, C., & Amy, L. A. (2007). Onset of submarine debris flow deposition far from original giant landslide. *Nature*, *450*, 541–544.

Tavani, S., Carola, E., Granado, P., Quintà, A., & Muñoz, J. A. (2013). Transpressive inversion of a Mesozoic extensional forced fold system with an intermediate décollement level in the Basque-Cantabrian Basin (Spain). *Tectonics*, *32*, 146–158.

Tindall, S. E., & Davis, G. H. (1999). Monocline development by oblique-slip fault-propagation folding: The East Kaibab monocline, Colorado Plateau, Utah. *Journal of Structural Geology*, *21*, 1303–1320.

Trauth, M. H., Maslin, M. A., Deino, A., & Strecker, M. R. (2005). Late Cenozoic moisture history of East Africa. *Science*, *1*, 1126. https://doi.org/10.1126/Science.1112964

Uno, K. T., Cerling, T. E., Harris, J. M., Kunimatsu, Y., Leakey, M. G., Nakatsukasa, M., & Nakaya, H. (2011). Late Miocene to Pliocene carbon isotope record of differential diet change among east African herbivores. *Proceedings of the National Academy of Sciences*, *108*, 6509–6514.

Veeken, P. C. H., & van Moerkerken, B. (2013). *Seismic stratigraphy and depositional facies models*. EAGE Publications.

Vendeville, B. (1987). *Champs de Failles et Tectonique en Extension: Modelization Expdrimentale* (PhD thesis). Universite de Rennes.

Vendeville, B. (1988). Mode1es experimentaux de fracturation de la couverture controlee par des failles normales dans le socle. *Comptes Rendus de l'Academie des Sciences, Paris*, *307*, 1013–1019.

Vendeville, B. C., Ge, H., & Jackson, M. P. A. (1995). Models of salt tectonics during basement extension. *Petroleum Geoscience*, *1*, 179–183.

Vormann, M., Franke, D., & Jokat, W. (2020). The crustal structure of the southern Davie ridge offshore northern Mozambique—A wide-angle seismic and potential field study. *Tectonophysics*, *778*, 228370. https://doi.org/10.1016/j.tecto2020.228370

Weimer, P., Slatt, R. M., Coleman, J. L., Rosen, N., Nelson, C. H., Bouma, A. H., Styzen, M., & Lawrence, D. T. (2000). Global deep-water reservoirs, *GCS-SEPM 20th Annual Research Conference*, 1104.

White, I. R., & Crider, J. G. (2006). Extensional fault propagation folds: Mechanical models and observations from the Modoc Plateau, northeastern California. *Journal of Structural Geology*, *28*, 1352–1370.

Willsey, S. P., Umhoefer, P. J., & Hilley, G. E. (2002). Early evolution of an extensional monocline by a propagating normal fault: 3D analysis from combined field study and numerical modelling. *Journal of Structural Geology*, *24*, 651–669.

Withjack, M. O., Meisling, K. E., & Russel, L. R. (1988). Forced folding and basement-detached normal faulting in the Haltenbaken area, offshore Norway. *AAPG Bulletin*, *72*, 259.

Withjack, M. O., Meisling, K. E., & Russel, L. R. (1989). Forced folding and basementnormal faulting in the Haltenbaken area, offshore Norway. *American Association of Petroleum Geologists, Memoir*, *46*, 567–575.

Withjack, M. O., Olson, J., & Peterson, E. (1990). Experimental models of extensional forced folds. *Bulletin of the American Association of Petroleum Geologists*, *74*, 1038–1054.

Wright, L. J. M., Muirhead, J. D., & Scholz, C. A. (2020). Spatiotemporal variations in upper crustal extension across the different basement terranes of the Lake Tanganyika Rift, East Africa. *Tectonics*, *39*, e2019TC006019. https://doi.org/10.1029/2019TC006019

Wu, N., Nugraha, H. D., Zhong, G. F., & Steventon, M. J. (2022). The role of mass-transport complexes in the initiation and evolution of submarine canyons. *Sedimentology*, *69*, 2181–2202. https://doi.org/10.1111/sed.12987

Yang, Z., & Chen, W. P. (2010). Earthquakes along the East African Rift system: A multiscale, system-wide perspective. *Journal of Geophysical Research, Solid Earth*, *115*(B12), B12309. https://doi.org/10.1029/2009JB006779

SUPPORTING INFORMATION

Additional supporting information can be found online in the Supporting Information section at the end of this article.

How to cite this article: Dottore Stagna, M., Maselli, V., Reynolds, D. J., Grujic, D., Iacopini, D., Reynolds, P., Tewari, S., & van Vliet, A. (2024). Re-routing of submarine channels by Plio-Quaternary extensional tectonics along the Tanzania margin and implications for an offshore branch of the East African Rift System. *Basin Research*, *36*, e12878. https://doi.org/10.1111/bre.12878